Clemens, S.C., Kuhnt, W., LeVay, L.J., and the Expedition 353 Scientists *Proceedings of the International Ocean Discovery Program* Volume 353 publications.iodp.org



doi:10.14379/iodp.proc.353.108.2016

Site U14481



S.C. Clemens, W. Kuhnt, L.J. LeVay, P. Anand, T. Ando, M. Bartol, C.T. Bolton, X. Ding, K. Gariboldi, L. Giosan, E.C. Hathorne, Y. Huang, P. Jaiswal, S. Kim, J.B. Kirkpatrick, K. Littler, G. Marino, P. Martinez, D. Naik, A. Peketi, S.C. Phillips, M.M. Robinson, O.E. Romero, N. Sagar, K.B. Taladay, S.N. Taylor, K. Thirumalai, G. Uramoto, Y. Usui, J. Wang, M. Yamamoto, and L. Zhou²

Keywords: International Ocean Discovery Program, IODP, Expedition 353, *JOIDES Resolution*, Site U1448, Indian monsoon, monsoon, Bay of Bengal, Andaman Sea, paleoclimate, paleoceanography, Miocene, Pliocene, Pleistocene, Holocene, Ninetyeast Ridge, Indian Ocean, salinity, orbital, millennial, centennial, abrupt climate change

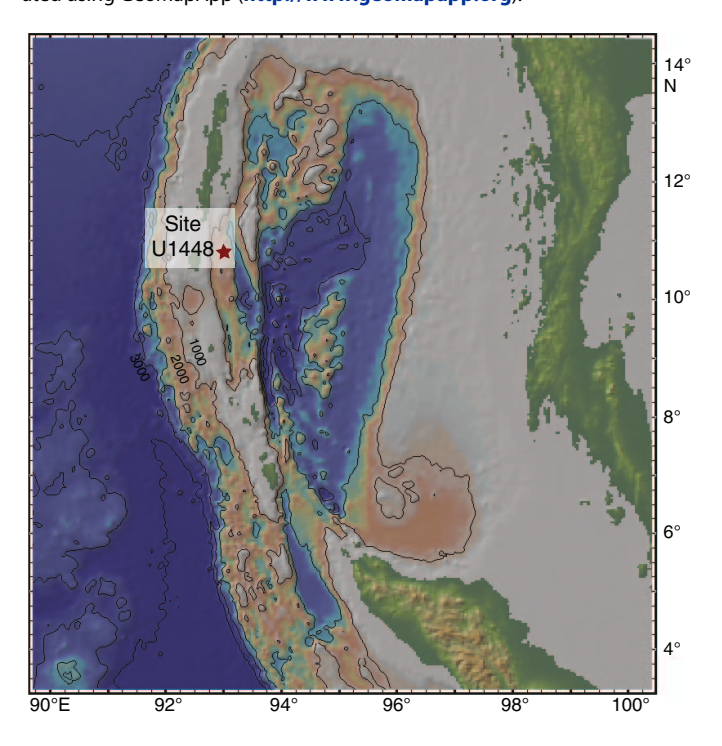
Contents

- Background and objectives
- 2 Operations
- 5 Lithostratigraphy
- **10** Biostratigraphy
- **15** Geochemistry
- **18** Paleomagnetism
- **22** Physical properties
- **26** Stratigraphic correlation
- 27 References

Background and objectives

The Andaman Sea is situated between the Andaman Islands and the Malay Peninsula (Figure F1). The Andaman-Sumatra island arc system results from the oblique subduction of the Indo-Australian plate beneath the Eurasian plate (Singh et al., 2013). Stretching and rifting of the overriding plate during the early Miocene (~25 Ma)

Figure F1. Andaman Sea map with location of Site U1448. Map was generated using GeoMapApp (http://www.geomapapp.org).



resulted in two distinct plates (Sunda and Burma) separated by an active spreading center (Curray, 1991, 2005) located in the deepest portion of the Andaman Sea. An accretionary wedge complex scraped off the subducting slab lies west of the spreading center, forming a series of shallower basins associated with backthrust faulting within the accreted sediments (Figure F2). The Andaman Sea drilling sites are within the Nicobar-Andaman Basin, bounded on either side by the Diligent and Eastern margin faults.

Runoff into the Andaman Sea is dominated by the Irrawaddy and Salween Rivers (Varkey et al., 1996), supplying a combined 30.8 × 10¹⁰ m³ of water during June, July, and August. Comparison with the winter (December, January, and February) discharge of 2.8 × 1010 m3 indicates strong seasonality with a dominance of summer (92%) over winter (8%) runoff. Terrigenous sediment supply to the Andaman Sea is dominantly from the Irrawaddy and Salween Rivers (Colin et al., 1999, 2006) with contributions from the Indo-Burman-Arakan mountain ranges as well as the Andaman Islands (Awasthi et al., 2014). However, by virtue of proximity, Little Andaman Island is likely a dominant source of terrigenous materials to International Ocean Discovery Program (IODP) Site U1448. Analysis of Andaman Sea surface sediments indicates that foraminifers are abundant and well preserved shallower than ~1800 meters below sea level (mbsl) (>100,000 individuals/g) and decrease to <100 individuals/g deeper than 3000 mbsl (Frerichs, 1971).

Site U1448 is located at 1091 mbsl, ~44 km offshore Little Andaman Island on a rise separating north-south—oriented basins associated with the Eastern margin and Diligent fault zones. Seismic sections (Figure F3) indicate ~420 m of sediments overlying an accretionary wedge complex. Sedimentation rates at Site NGHP-01-17 (Collett et al., 2008; Flores et al., 2014) suggest that this site should reach the late Miocene. Unlike IODP Site U1447, the elevated location of Site U1448 helps shield the site from turbidite deposition.

¹ Clemens, S.C., Kuhnt, W., LeVay, L.J., Anand, P., Ando, T., Bartol, M., Bolton, C.T., Ding, X., Gariboldi, K., Giosan, L., Hathorne, E.C., Huang, Y., Jaiswal, P., Kim, S., Kirkpatrick, J.B., Littler, K., Marino, G., Martinez, P., Naik, D., Peketi, A., Phillips, S.C., Robinson, M.M., Romero, O.E., Sagar, N., Taladay, K.B., Taylor, S.N., Thirumalai, K., Uramoto, G., Usui, Y., Wang, J., Yamamoto, M., and Zhou, L., 2016. Site U1448. *In* Clemens, S.C., Kuhnt, W., LeVay, L.J., and the Expedition 353 Scientists, *Indian Monsoon Rainfall*. Proceedings of the International Ocean Discovery Program, 353: College Station, TX (International Ocean Discovery Program). http://dx.doi.org/10.14379/iodp.proc.353.108.2016

Figure F2. Summary sketch after Singh et al. (2013) showing the subduction zone through the back-arc basin to \sim 40 km depth. DF = Diligent fault, NAB = Nicobar-Andaman Basin, ANF = Andaman-Nicobar fault.

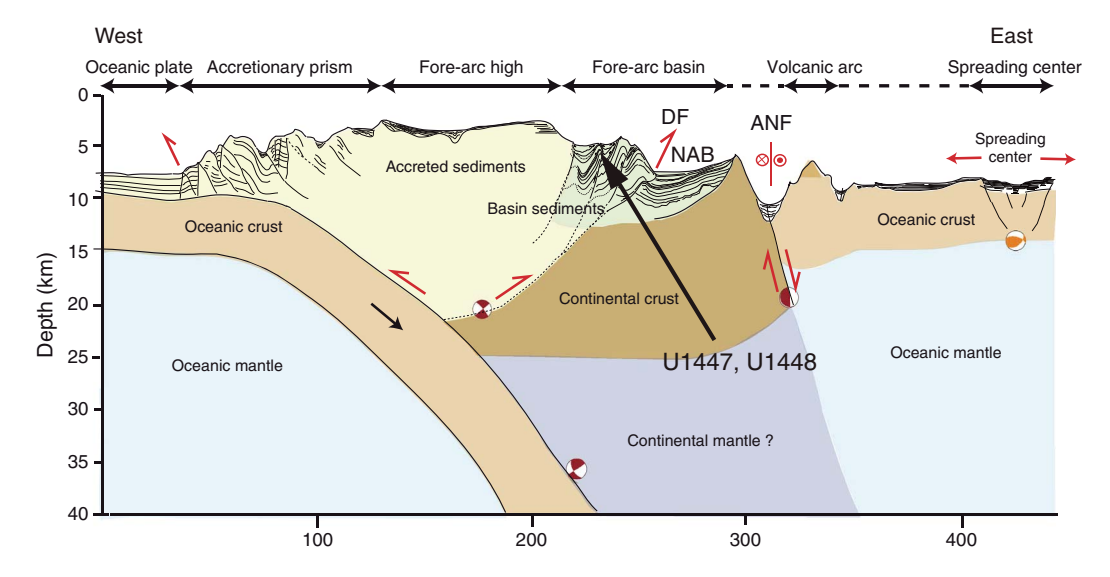
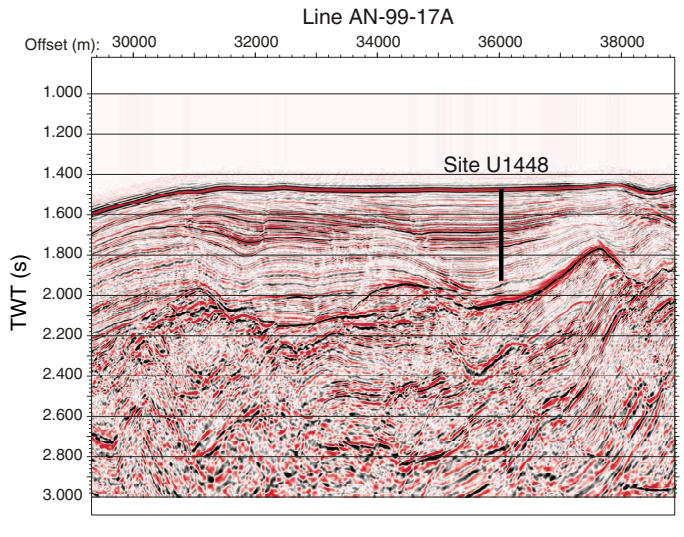
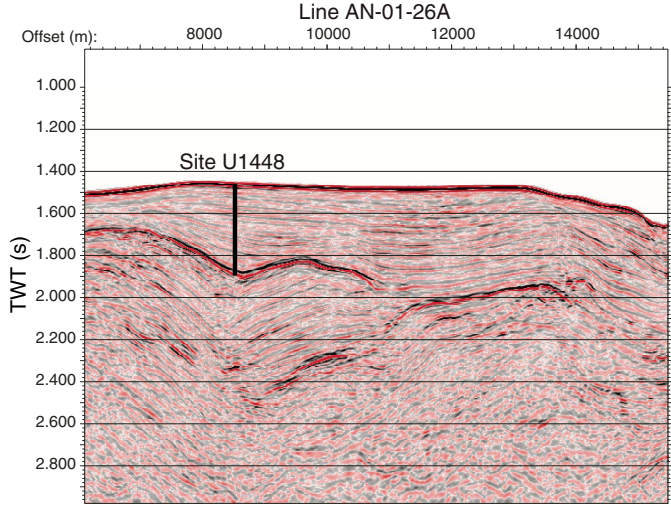


Figure F3. Seismic lines showing location of Site U1448. TWT = two-way traveltime.





The objective at this site is to recover Miocene to Holocene sediments from multiple holes in order to reconstruct changes in surface water salinity and runoff associated with summer monsoon rainfall at tectonic to suborbital timescales. Sites U1448 and U1447 constitute the middle (10°N) portion of a meridional salinity transect that includes sites on the northeast Indian margin (19°N) and is anchored by IODP Site U1443 at 5°N.

Operations

Site U1448 consisted of three holes (Table T1), ranging in depth from 34.3 to 421.0 m drilling depth below seafloor (DSF). Overall, 121 cores were recorded for the site. A total of 427.52 m of core over a 416.2 m cored interval was recovered using the advanced piston corer (APC) system (103% recovery). The cored interval with the half-length advanced piston corer (HLAPC) system was 318.6 m with a core recovery of 333.24 m (105%). The cored interval with the extended core barrel (XCB) system was 77.6 m with 78.21 m of core recovered (101%). The overall recovery percentage for Site U1448 was 103%. The total time spent on Site U1448 was 3.9 days.

Transit to Site U1448

The 9.4 nmi transit from Site U1447 to U1448 was completed in dynamic positioning mode with much of the transit being completed while the drill pipe was being pulled. The vessel arrived at Site U1448 at 1845 h (UTC + 8 h) on 21 January 2015. A positioning beacon was deployed at 1916 h, and the vessel settled over the site coordinates.

Hole U1448A

Hole U1448A was spudded at 0010 h on 22 January 2015. Core 353-U1448A-1H was used to estimate the seafloor depth at 1098.3 mbsl. The APC system was used for Cores 1H through 23H. Core 23H had no core recovery and was reshot from the same depth. The HLAPC was deployed for Cores 24F through 52F. Cores 53X through 60X were cut with the XCB system. Downhole temperature measurements were attempted using the advanced piston corer temperature tool (APCT-3) shoe, but when it was deployed for Core

Table T1. Site U1448 core summary. CSF = core depth below seafloor, DRF = drilling depth below rig floor, DSF = drilling depth below seafloor, mbsl = meters below sea level. F = half-length advanced piston corer, H = advanced piston corer, X = extended core barrel, numeric core type = drilled interval. (Continued on next two pages.) **Download table in .csv format.**

Hole U1448A

Latitude: 10°38.0315′N Longitude: 93°00.0036′E Time on hole (h): 47.75

Seafloor (drill pipe measurement below rig floor, m DRF): 1109.7

Distance between rig floor and sea level (m): 11.4

Water depth (drill pipe measurement from sea level, mbsl): 1098.3

Total penetration (drilling depth below seafloor, m DSF): 421

Total length of cored section (m): 421 Total core recovered (m): 434.82 Core recovery (%): 103 Total number of cores: 60

Hole U1448C

Latitude: 10°38.0830'N Longitude: 93°00.0233'E Time on hole (h): 9.25

Seafloor (drill pipe measurement below rig floor, m DRF): 1108.2

Distance between rig floor and sea level (m): 11.4

Water depth (drill pipe measurement from sea level, mbsl): 1096.8 Total penetration (drilling depth below seafloor, m DSF): 34.3

Total length of cored section (m): 34.3 Total core recovered (m): 34.77 Core recovery (%): 101 Total number of cores: 4

Hole U1448B

Latitude: 10°38.0202′N Longitude: 93°00.0032′E Time on hole (h): 36

Seafloor (drill pipe measurement below rig floor, m DRF): 1107.9

Distance between rig floor and sea level (m): 11.4

Water depth (drill pipe measurement from sea level, mbsl): 1096.5 Total penetration (drilling depth below seafloor, m DSF): 358.6

Total length of cored section (m): 357.1 Total core recovered (m): 369.38

Core recovery (%): 103 Total number of cores: 57

			Depth	DSF (m)		Depth	CSF (m)			
Core	Date (2015)	Time UTC (h)	Top of cored interval	Bottom of cored interval	Interval advanced (m)	Top of cored interval	Bottom of cored interval	Length of core recovered (m)	Recovery (%)	Sections (N)
353-U144	8A-									
1H	21 Jan	1620	0.0	2.4	2.4	0.0	2.47	2.47	103	3
2H	21 Jan	1650	2.4	11.9	9.5	2.4	12.14	9.74	103	8
3H	21 Jan	1715	11.9	21.4	9.5	11.9	21.62	9.72	102	8
4H	21 Jan	1755	21.4	30.9	9.5	21.4	31.46	10.06	106	8
5H	21 Jan	1825	30.9	40.4	9.5	30.9	40.78	9.88	104	8
6H	21 Jan	1855	40.4	49.9	9.5	40.4	50.08	9.68	102	8
7H	21 Jan	1930	49.9	59.4	9.5	49.9	59.78	9.88	104	8
8H	21 Jan	2000	59.4	68.9	9.5	59.4	69.39	9.99	105	8
9H	21 Jan	2030	68.9	78.4	9.5	68.9	78.81	9.91	104	8
10H	21 Jan	2100	78.4	87.9	9.5	78.4	88.34	9.94	105	8
11H	21 Jan	2130	87.9	97.4	9.5	87.9	97.77	9.87	104	8
12H	21 Jan	2205	97.4	106.9	9.5	97.4	107.24	9.84	104	8
13H	21 Jan	2245	106.9	116.4	9.5	106.9	116.57	9.67	102	7
14H	21 Jan	2305	116.4	125.9	9.5	116.4	126.48	10.08	106	8
15H	21 Jan	2335	125.9	135.4	9.5	125.9	135.65	9.75	103	8
16H	22 Jan	0010	135.4	144.9	9.5	135.4	145.41	10.01	105	8
17H	22 Jan	0045	144.9	154.4	9.5	144.9	154.97	10.07	106	8
18H	22 Jan	0115	154.4	163.9	9.5	154.4	164.39	9.99	105	8
19H	22 Jan	0200	163.9	173.4	9.5	163.9	173.67	9.77	103	8
20H	22 Jan	0230	173.4	182.9	9.5	173.4	183.11	9.71	102	8
21H	22 Jan	0305	182.9	192.4	9.5	182.9	191.92	9.02	95	7
22H	22 Jan	0340	192.4	195.9	3.5	192.4	195.92	3.52	101	4
23H	22 Jan	0515	195.9	204.2	8.3	195.9	204.32	8.42	101	7
24F	22 Jan	0620	204.2	209.0	4.8	204.2	209.25	5.05	105	5
25F	22 Jan	0650	209.0	213.8	4.8	209.0	214.11	5.11	106	5
26F	22 Jan	0715	213.8	218.6	4.8	213.8	218.86	5.06	105	5
27F	22 Jan	0740	218.6	223.4	4.8	218.6	223.66	5.06	105	5
28F	22 Jan	0825	223.4	228.2	4.8	223.4	228.41	5.01	104	5
29F	22 Jan	0950	228.2	233.0	4.8	228.2	233.27	5.07	106	5
30F	22 Jan	1015	233.0	237.8	4.8	233.0	238.12	5.12	107	5
31F	22 Jan	1040	237.8	242.6	4.8	237.8	242.87	5.07	106	5
32F	22 Jan	1110	242.6	247.4	4.8	242.6	247.68	5.08	106	5
33F	22 Jan	1140	247.4	252.2	4.8	247.4	252.47	5.07	106	5
34F	22 Jan	1200	252.2	257.0	4.8	252.2	257.21	5.01	104	5
35F	22 Jan	1225	257.0	261.8	4.8	257.0	262.03	5.03	105	5
36F	22 Jan	1250	261.8	266.6	4.8	261.8	266.79	4.99	104	5
37F	22 Jan	1315	266.6	271.4	4.8	266.6	271.49	4.89	102	5
38F	22 Jan	1340	271.4	276.2	4.8	271.4	276.35	4.95	103	5
39F	22 Jan	1400	276.2	281.0	4.8	276.2	281.17	4.97	104	5

Table T1 (continued). (Continued on next page.)

			Depth	DSF (m)		Depth	n CSF (m)	=		
Core	Date (2015)	Time UTC (h)	Top of cored interval	Bottom of cored interval	Interval advanced (m)	Top of cored interval	Bottom of cored interval	Length of core recovered (m)	Recovery (%)	Sections (N)
40F	22 Jan	1425	281.0	285.8	4.8	281.0	286.02	5.02	105	5
41F	22 Jan	1450	285.8	290.6	4.8	285.8	290.72	4.92	103	5
42F	22 Jan	1515	290.6	295.4	4.8	290.6	295.57	4.97	104	5
43F	22 Jan	1535	295.4	300.2	4.8	295.4	300.43	5.03	105	5
44F	22 Jan	1610	300.2	305.0	4.8	300.2	305.40	5.20	108	5
45F	22 Jan	1700	305.0	309.8	4.8	305.0	310.08	5.08	106	5
46F	22 Jan	1750	309.8	314.6	4.8	309.8	314.94	5.14	107	5
47F	22 Jan	1820	314.6	319.4	4.8	314.6	319.69	5.09	106	5
48F	22 Jan	1850	319.4	324.2	4.8	319.4	324.60	5.20	108	5
49F	22 Jan	1925	324.2	329.0	4.8	324.2	328.56	4.36	91	4
50F	22 Jan	2000	329.0	333.8	4.8	329.0	334.27	5.27	110	5
51F	22 Jan	2045	333.8	338.6	4.8	333.8	338.60	4.80	100	6
52F	22 Jan	2140	338.6	343.4	4.8	338.6	343.60	5.00	104	5
53X	23 Jan	0045	343.4	353.1	9.7	343.4	353.33	9.93	102	8
54X	23 Jan	0155	353.1	362.8	9.7	353.1	362.98	9.88	102	8
55X	23 Jan	0305	362.8	372.5	9.7	362.8	372.64	9.84	101	8
56X	23 Jan	0420	372.5	382.2	9.7	372.5	382.24	9.74	100	8
57X	23 Jan 23 Jan	0520	382.2	391.9	9.7	382.2	392.00	9.80	101	8
58X		0615	391.9	401.6	9.7	391.9	401.81	9.91	102	8
59X 60X	23 Jan	0720	401.6	411.3	9.7 9.7	401.6	411.41	9.81	101 96	8 9
353-U1448	23 Jan 8B-	0825	411.3	421.0	9.7	411.3	420.60	9.30	96	9
1H	23 Jan	1215	0.0	8.6	8.6	0.0	8.60	8.60	100	7
2H	23 Jan	1255	8.6	18.1	9.5	8.6	18.24	9.64	101	8
3H	23 Jan	1320	18.1	27.6	9.5	18.1	27.68	9.58	101	8
4H	23 Jan	1400	27.6	36.1	8.5	27.6	37.30	9.70	114	8
5H	23 Jan	1430	36.1	45.6	9.5	36.1	45.83	9.73	102	8
6H	23 Jan	1500	45.6	55.1	9.5	45.6	55.41	9.81	103	8
7H	23 Jan	1550	55.1	64.6	9.5	55.1	65.06	9.96	105	8
8H	23 Jan	1620	64.6	74.1	9.5	64.6	74.38	9.78	103	8
9H	23 Jan	1650	74.1	83.6	9.5	74.1	83.92	9.82	103	8
10H	23 Jan	1735	83.6	93.1	9.5	83.6	93.60	10.00	105	8
11H	23 Jan	1805	93.1	102.6	9.5	93.1	103.01	9.91	104	8
12H	23 Jan	1835	102.6	112.1	9.5	102.6	112.49	9.89	104	8
13H	23 Jan	1905	112.1	121.6	9.5	112.1	121.70	9.60	101	7
14H	23 Jan	1940	121.6	131.1	9.5	121.6	130.03	8.43	89	7
15H	23 Jan	2035	131.1	140.6	9.5	131.1	141.16	10.06	106	8
16H	23 Jan	2115	140.6	150.1	9.5	140.6	150.37	9.77	103	8
17H	23 Jan	2145	150.1	159.6	9.5	150.1	159.42	9.32	98	7
18H	23 Jan	2230	159.6	168.2	8.6	159.6	168.25	8.65	101	7
19H	23 Jan	2335	168.2	177.7	9.5	168.2	177.71	9.51	100	8
201	24 Jan	0045			*****Dr	illed interval 17	7.7-179.2 m DSF**	***		
21F	24 Jan	0055	179.2	184.0	4.8	179.2	184.28	5.08	106	5
22F	24 Jan	0125	184.0	188.8	4.8	184.0	188.97	4.97	104	5
23F	24 Jan	0150	188.8	193.6	4.8	188.8	193.84	5.04	105	5
24F	24 Jan	0235	193.6	198.4	4.8	193.6	198.63	5.03	105	5
25F	24 Jan	0305	198.4	203.2	4.8	198.4	203.47	5.07	106	5
26F	24 Jan	0330	203.2	208.0	4.8	203.2	208.25	5.05	105	5
27F	24 Jan	0355	208.0	212.8	4.8	208.0	213.06	5.06	105	5
28F	24 Jan	0415	212.8	217.6	4.8	212.8	217.84	5.04	105	5
29F	24 Jan	0505	217.6	222.4	4.8	217.6	222.68	5.08	106	5
30F	24 Jan	0530	222.4	227.2	4.8	222.4	227.42	5.02	105	5
31F	24 Jan	0555	227.2	230.0	2.8	227.2	231.04	3.84	137	4
32F	24 Jan	0620	230.0	234.8	4.8	230.0	235.00	5.00	104	5
33F	24 Jan	0640	234.8	238.6	3.8	234.8	239.13	4.33	114	4
34F	24 Jan	0705	238.6	243.4	4.8	238.6	243.61	5.01	104	5
35F	24 Jan	0740	243.4	248.2	4.8	243.4	248.52	5.12	107	5
36F	24 Jan	0800	248.2	253.0	4.8	248.2	253.28	5.12	106	5
37F	24 Jan	0825	253.0	257.8	4.8	253.0	258.09	5.09	106	5
38F	24 Jan	0855	257.8	262.6	4.8	257.8	262.91	5.11	106	5
39F	24 Jan	0920	262.6	267.4	4.8	262.6	267.64	5.04	105	5
40F	24 Jan	0950	267.4	272.2	4.8	267.4	272.56	5.16	108	5
41F	24 Jan	1015	272.2	277.0	4.8	272.2	277.26	5.06	105	5
42F	24 Jan	1045	277.0	281.8	4.8	277.0	282.04	5.04	105	5
43F	24 Jan	1110	281.8	286.6	4.8	281.8	286.90	5.10	106	5
44F	24 Jan	1135	286.6	291.4	4.8	286.6	291.71	5.11	106	5
45F	24 Jan	1155	291.4	296.2	4.8	291.4	296.46	5.06	105	5
46F			296.2	301.0	4.8	296.2	301.31	5.11		5

Table T1 (continued).

			Depth	DSF (m)		Depth	CSF (m)			
Core	Date (2015)	Time UTC (h)	Top of cored interval	Bottom of cored interval	Interval advanced (m)	Top of cored interval	Bottom of cored interval	Length of core recovered (m)	Recovery (%)	Sections (N)
47F	24 Jan	1255	301.0	305.8	4.8	301.0	306.19	5.19	108	5
48F	24 Jan	1320	305.8	310.6	4.8	305.8	310.86	5.06	105	5
49F	24 Jan	1435	310.6	315.4	4.8	310.6	315.72	5.12	107	5
50F	24 Jan	1505	315.4	320.2	4.8	315.4	320.43	5.03	105	5
51F	24 Jan	1530	320.2	325.0	4.8	320.2	325.34	5.14	107	5
52F	24 Jan	1600	325.0	329.8	4.8	325.0	330.03	5.03	105	5
53F	24 Jan	1635	329.8	334.6	4.8	329.8	333.69	3.89	81	5
54F	24 Jan	1745	334.6	339.4	4.8	334.6	339.66	5.06	105	5
55F	24 Jan	1815	339.4	344.2	4.8	339.4	344.55	5.15	107	5
56F	24 Jan	1855	344.2	349.0	4.8	344.2	348.31	4.11	86	4
57F	24 Jan	1935	349.0	353.8	4.8	349.0	353.72	4.72	98	4
58F	24 Jan	2100	353.8	358.6	4.8	353.8	358.22	4.42	92	4
353-U144	8C-									
1H	25 Jan	0000	0.0	5.8	5.8	0.0	5.83	5.83	101	4
2H	25 Jan	0030	5.8	15.3	9.5	5.8	15.24	9.44	99	8
3H	25 Jan	0050	15.3	24.8	9.5	15.3	24.89	9.59	101	8
4H	25 Jan	0125	24.8	34.3	9.5	24.8	34.71	9.91	104	8

4H, the reading was bad. The Icefield MI-5 tool was used to obtain orientation data for Cores 3H through 23H. At the end of coring operations, the drill pipe was pulled from the hole and cleared the seafloor at 1830 h on 23 January.

A total of 23 APC cores were taken over a 204.2 m interval with a total core recovery of 210.99 m (103% core recovery). The HLAPC system was used for 29 cores over a cored interval of 139.2 m with 145.62 m recovered (105%). A total of 8 XCB cores were cut over a 77.6 m interval with 78.21 m of core recovered (101%). Total core recovery for Hole U1448A was 103%.

Hole U1448B

The vessel was offset 20 m south of Hole U1448A, and Hole U1448B was spudded at 2010 h on 23 January 2015. Cores 353-U1448B-1H through 19H were recovered using the APC system. Before switching to the HLAPC system, the hole was advanced 1.5 m without coring. The HLAPC was used for Cores 21F through 58F. Temperature measurements using the APCT-3 were taken on Cores 4H, 7H, 10H, and 15H. Cores 3H through 19H were oriented using the Icefield MI-5 tool. The drill string was then pulled from the hole and the bit cleared the seafloor at 0630 h on 25 January, ending Hole U1448B.

A total of 19 APC cores were taken over a 177.7 m interval with a total core recovery of 181.76 m (102% core recovery). The HLAPC system was used for 38 cores that were taken over a 179.4 m interval with 187.62 m of core recovered (105%). One drilled interval of 1.5 m (353-U1448B-201) was recorded for the hole. Total core recovery for Hole U1448B was 103%.

Hole U1448C

The vessel was offset 20 m west of Hole U1448B, and Hole U1448C was spudded at 0750 h on 25 January 2015. Cores 353-U1448C-1H through 4H were cored with the APC system to a total depth of 34.3 m DSF. The drill string was then pulled from the hole with the bit clearing the seafloor at 1000 h, and the rig was secured for transit to Singapore.

A total of four APC cores were taken over a 34.3 m cored interval with a total core recovery of 34.77 m (101% core recovery).

Transit to Loyang, Singapore

The vessel began transit to Singapore at 1542 h on 25 January 2015. The vessel arrived at the Singapore pilot station at 0811 h on 29 January 2015, after a 904 nmi transit, where Expedition 353 officially ended.

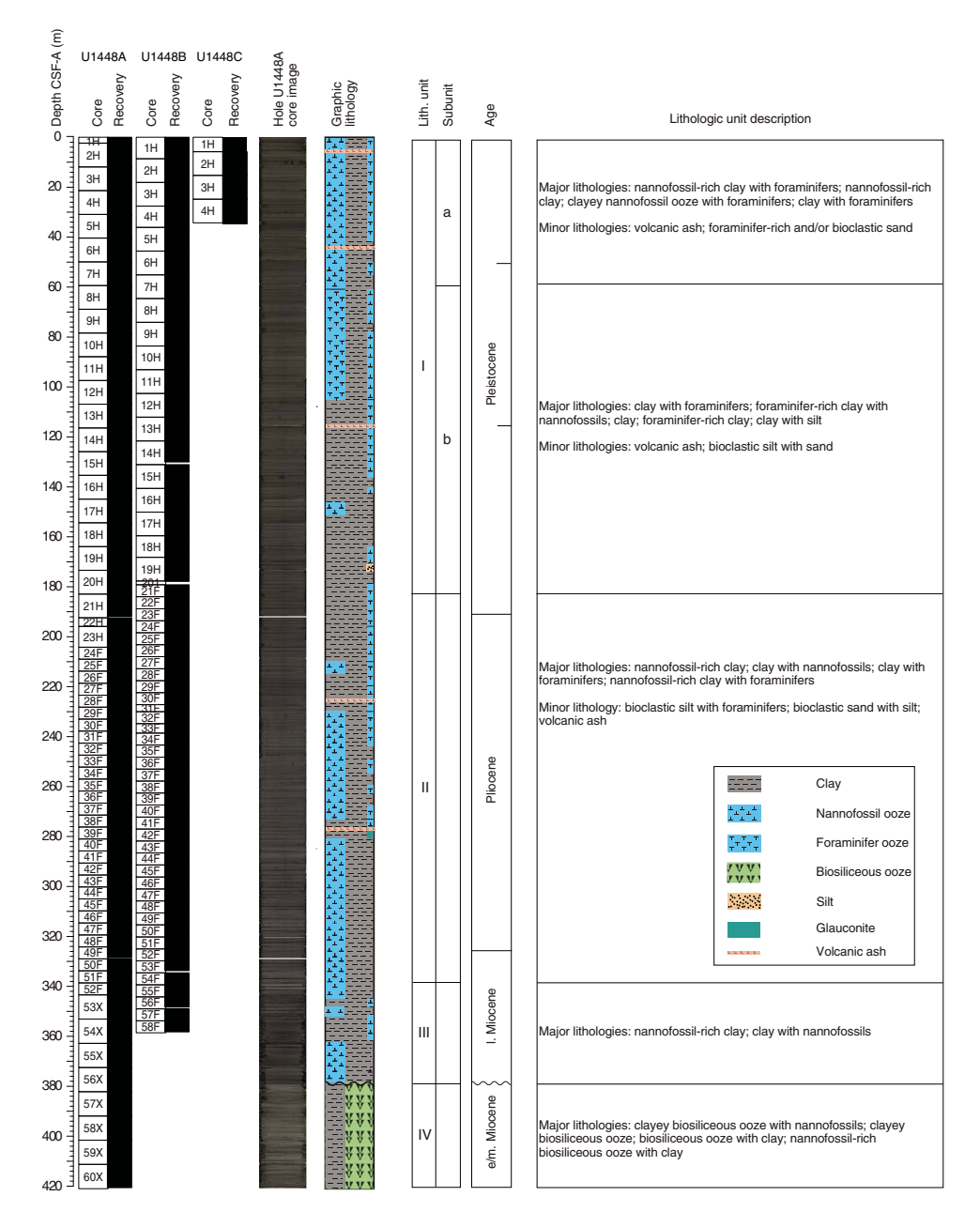
Lithostratigraphy

Sediments recovered from Holes U1448A-U1448C are principally composed of Late Pleistocene to middle Miocene hemipelagic sediments with a significant clay and biogenic component, comprising four distinct lithostratigraphic units (I-IV) (Figure F4). The observed lithologic differences between units are primarily the result of varying abundances of bioclastics (nannofossils, foraminifers, diatoms, and sponge spicules), clay, and glauconite (Figure F5). Unit I is 180 m thick and composed of Late to early Pleistocene greenish gray clay with varying proportions of nannofossils and foraminifers, as well as clayey nannofossil ooze. Unit II is 160 m thick and composed of early Pleistocene to late Miocene greenish clay with varying proportions of nannofossils and foraminifers and is characterized by low biosilica content (≤1%). Unit III is 40 m thick and composed of late Miocene greenish dark to light gray nannofossil-rich clay and clay with nannofossils, characterized by increased abundance of glauconite (up to 7%) and siliceous sponge spicules (up to 4%). A hiatus representing ~8 My occurs at the base of Unit III at 379.11 m core depth below seafloor, Method A (CSF-A), where there is an abrupt change in lithology that defines the top of Unit IV. Unit IV is composed of middle to early Miocene greenish gray to light greenish gray biosiliceous ooze with varying proportions of clay and nannofossils. Lithologic descriptions are based primarily on sediments recovered from Hole U1448A, supplemented with observations from Hole U1448B.

Unit I

Intervals: 353-U1448A-1H-1, 0 cm, through 20H-CC, 29 cm; 353-U1448B-1H-1, 0 cm, through 21F-CC, 29 cm; 353-U1448C-1H-1, 0 cm, through 4H-CC, 17 cm

Figure F4. Lithostratigraphic summary, Site U1448. All unit divisions are plotted relative to Hole U1448A. Details of each core are available in the visual core description logs.



Depths: Hole U1448A = 0-183.11 m CSF-A; Hole U1448B = 0-184.28 m CSF-A; Hole U1448C = 0-34.71 m CSF-A

Age: early Pleistocene to Late Pleistocene

Lithology: nannofossil-rich clay, clayey nannofossil ooze, foraminifer-rich clay, and clay

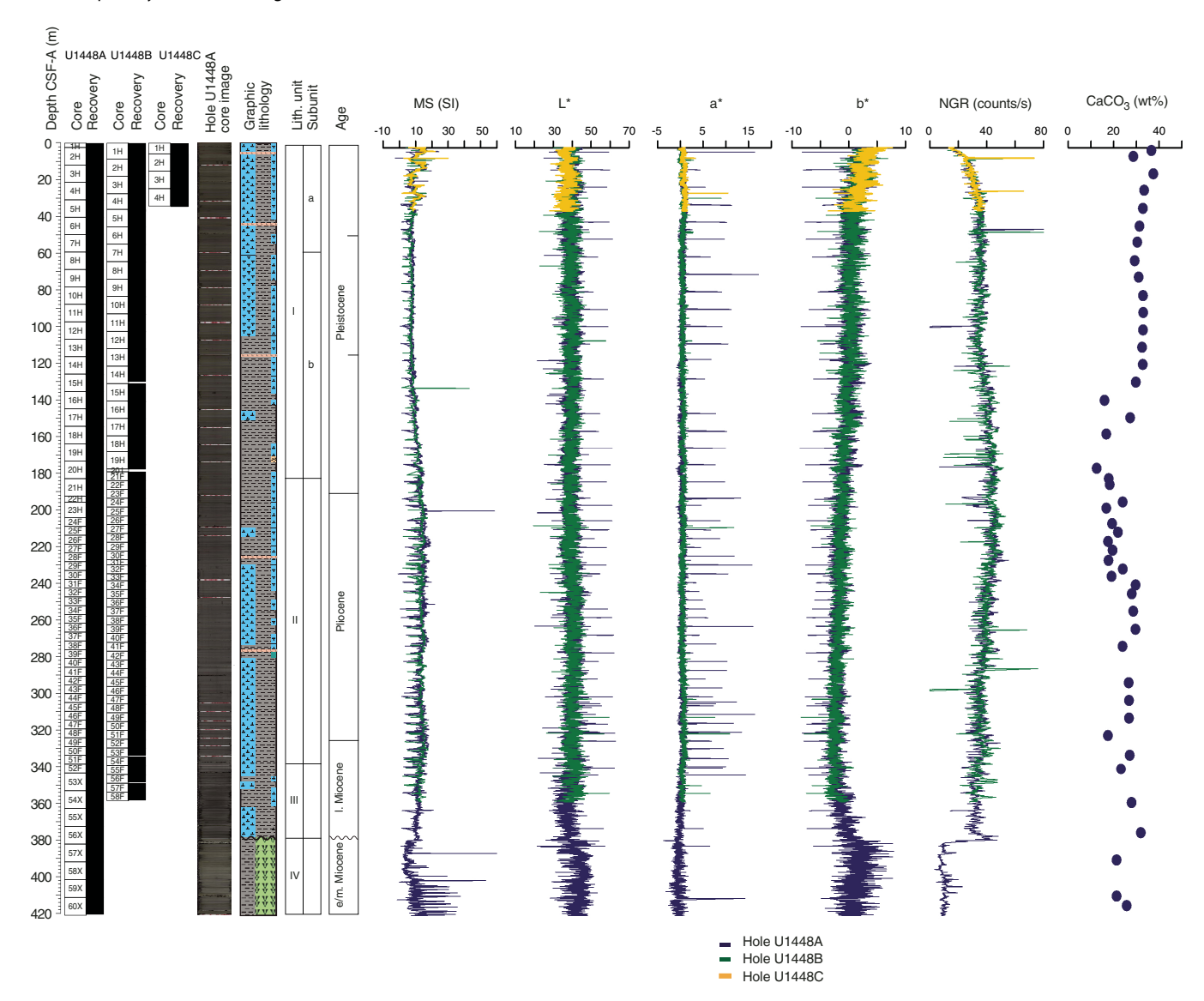
Unit I is a \sim 180 m thick succession of dark greenish gray to greenish gray (GLEY 1 4/10Y–6/10Y, GLEY 1 5GY series, and GLEY 1 10GY series) clay with varying proportions of nannofossils and foraminifers, as well as clayey nannofossil ooze (Figures **F4**, **F6**, **F7**, **F8**). Clay composes \sim 40%–60% of the sediment followed by calcareous nannofossils (20%–40%), foraminifers (10%–30%), and siliceous sponge spicules (up to 5%) (Figure **F6**). The proportion of clay increases downhole, reflected in the increasing natural gamma radia-

tion (NGR) values (Figure F5) (see Physical properties). Turbidites and ash layers are rarely observed. The Unit I/II boundary is defined by changes in the proportion of nannofossils and biosilica (Figure F6). Unit I is divided into two subunits. Subunit Ib is distinguished from Subunit Ia by a decrease in nannofossils and increase in siliceous sponge spicules.

Subunit la

Intervals: 353-U1448A-1H-1, 0 cm, through 7H-CC, 25 cm; 353-U1448B-1H-1, 0 cm, through 7H-4, 147 cm; 353-U1448C-1H-1, 0 cm, through 4H-CC, 17 cm Depths: Hole U1448A = 0-59.78 m CSF-A; Hole U1448B = 0-60.99 m CSF-A; Hole U1448C = 0-34.71 m CSF-A

Figure F5. Lithostratigraphic summary with selected physical property and geochemical data from Holes U1448A–U1448C plotted against depth. MS = magnetic susceptibility, NGR = natural gamma radiation.



Age: Late Pleistocene

Major lithology: nannofossil-rich clay with foraminifers, nannofossil-rich clay, clayey nannofossil ooze with foraminifers, and clay with foraminifers

Minor lithology: volcanic ash and foraminifer-rich and/or bioclastic sand

Subunit Ia is a ~60 m thick succession of light greenish gray (GLEY 1 5/10Y) nannofossil-rich clay with foraminifers, nannofossil-rich clay, clayey nannofossil ooze with foraminifers, and clay with foraminifers (Figures F4, F6, F7). Clays make up ~40%–60% of the sediment in Subunit Ia, followed by calcareous nannofossils (20%–40%), and foraminifers (~10%–20%) (Figure F6). Turbiditic beds composed of 2–7 cm thick bioclastic sands with normal grading are rarely observed. Two thick vitric ash layers are present in sediments from Subunit Ia (Figure F8). A light gray ash at 5.85–6.09 m CSF-A in Hole U1448A, 5.53–6.09 m CSF-A in Hole U1448B, and 5.71–5.83 m CSF-A in Hole U1448C is likely associated with the Toba eruption during the Late Pleistocene (Figures F8C, F9A).

Some dark gray blebs and nodules of iron sulfides are observed. Drilling disturbance is minor with occasional horizontal cracks, fallin, and soupy textures.

Subunit Ib

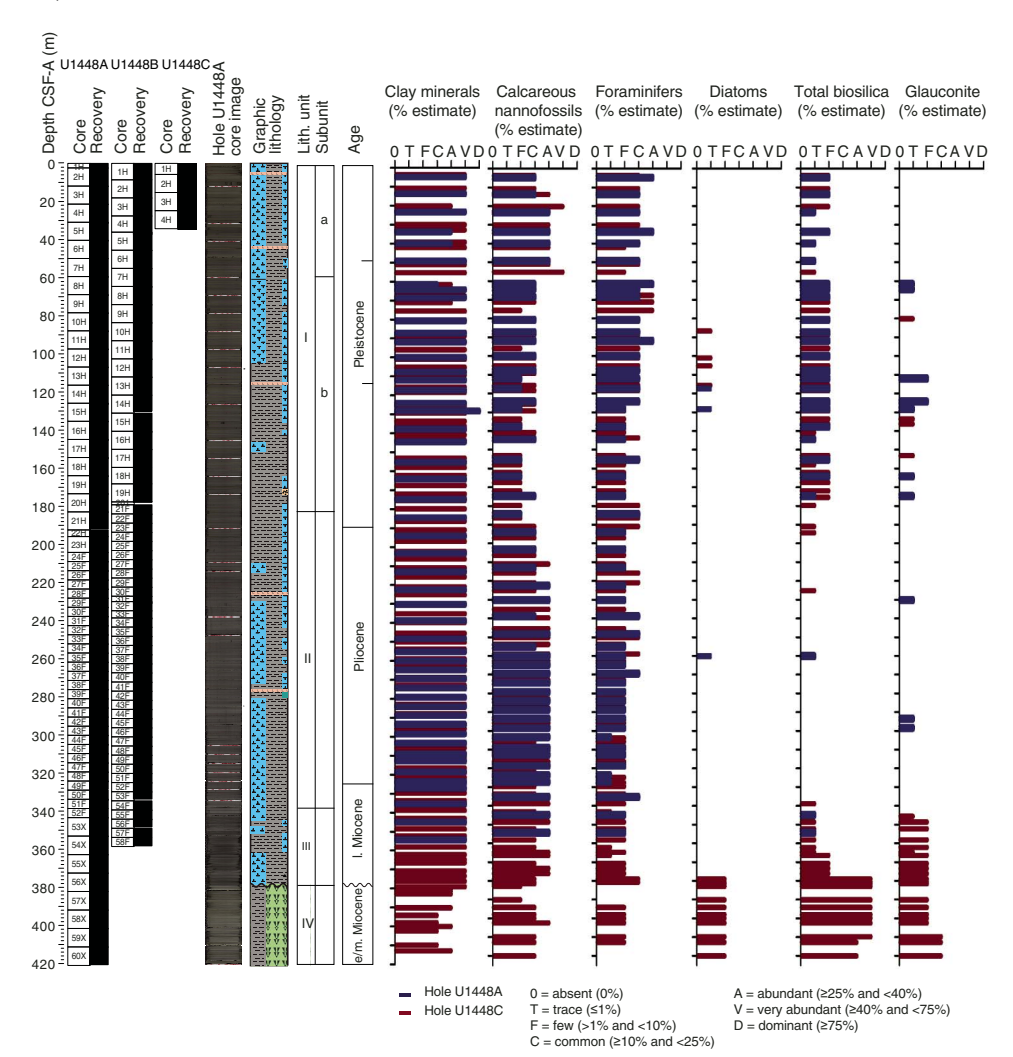
353-U1448B-7H-5, 0 cm, through 21F-CC, 29 cm
Depths: Hole U1448A = 59.78–183.11 m CSF-A;
Hole U1448B = 60.99–184.28 m CSF-A
Age: early Pleistocene to Middle Pleistocene
Major lithology: clay with foraminifers, foraminifer-rich clay with

Intervals: 353-U1448A-8H-1, 0 cm, through 20H-CC, 29 cm;

nannofossils, clay, foraminifer-rich clay, and clay with silt Minor lithology: volcanic ash and bioclastic silt with sand

Subunit Ib is a \sim 120 m thick succession of dark greenish gray to greenish gray (GLEY 1 4/10Y–6/10Y, GLEY 1 5GY series, and GLEY 1 10GY series) nannofossil-rich clay with foraminifers, nannofossil-rich clay, clayey nannofossil ooze with foraminifers, and clay with

Figure F6. Smear slide data, Holes U1448A and U1448C.



foraminifers (Figures **F4**, **F5**, **F6**, **F7**). Clays compose ~40%–60% of Subunit Ib, followed by calcareous nannofossils (20%–40%), foraminifers (~10%–20%), and siliceous sponge spicules (up to 5%). Proportions of foraminifers show a gradual decrease from ~30% to ~10% through this unit, with calcareous nannofossils showing a similar decline (Figure **F6**). A 0.5 cm thick turbidite and a 3 cm thick ash layer are observed, as well as some dark gray blebs and nodules of iron sulfides. Punctures caused by a deformed liner are the only minor drilling disturbance.

Unit II

Intervals: 353-U1448A-21H-1, 0 cm, through 51F-CC, 21 cm; 353-U1448B-22F-1, 0 cm, through 55F-CC, 23 cm Depths: Hole U1448A = 183.11–338.60 m CSF-A;

Hole U1448B = 184.28–344.55 m CSF-A

Age: late Miocene to late Pliocene

Major lithology: nannofossil-rich clay, clay with nannofossils, clay with foraminifers, and nannofossil-rich clay with foraminifers

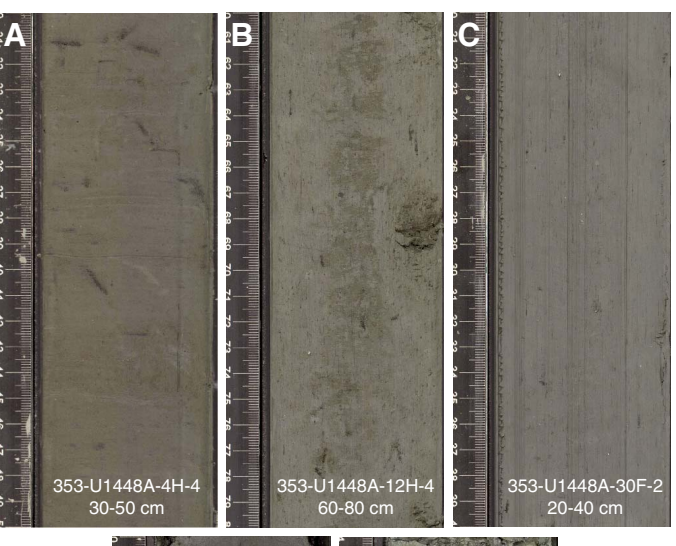
Minor lithology: bioclastic silt with foraminifers, bioclastic sand with silt, and volcanic ash

Unit II is a ~160 m thick succession of greenish gray (GLEY 1 4/10Y-6/10Y, GLEY 15GY series, and GLEY 110GY series) nannofossil-rich clay, clay with nannofossils, clay with foraminifers, and nannofossil-rich clay with foraminifers (Figures F7, F8). Clay composes ~50%-70% of the sediment followed by calcareous nannofossils (10%-30%) and foraminifers (up to 18%) (Figure F6). The sediments are low in biosilica (≤1%) and are dominated by diatoms (Figure F6). Proportions of nannofossils show a gradual increase downcore from ~10% to ~30% in the upper 100 m interval of this unit. Beds of bioclastic silt, 1.5–6 cm thick, with normal grading are rarely observed and are likely turbidites. Ash layers are rare, but a ~12 cm thick pinkish gray (7.5YR 7/2) ash is observed at 225.71-225.83 m CSF-A in Hole U1448A and 228.00-228.125 m CSF-A in Hole U1448B. Centimeter-scale pyrite nodules and pyritized wood fragments are observed. The Unit II/III boundary is defined by changes in color and biosilica content. Drilling disturbance is minor with occasional horizontal cracks, fragmented textures, and fall-in within Unit II.

Unit III

Intervals: 353-U1448A-52F-1, 0 cm, through 56X-5, 60 cm; 353-U1448B-56F-1, 0 cm, through 58F-CC, 8 cm

Figure F7. Line-scan images of main lithologies, Site U1448. A. Nannofossilrich clay with foraminifers, Subunit Ia. B. Foraminifer-rich clay, Subunit Ib. C. Nannofossil-rich clay with foraminifers, Unit II. D. Clay with nannofossils, Unit III. E. Clayey biosiliceous ooze, Unit IV.





Depths: Hole U1448A = 338.60–379.11 m CSF-A; Hole U1448B = 344.55–358.22 m CSF-A Age: late Miocene

Major lithology: nannofossil-rich clay and clay with nannofossils

Unit III is a ~40 m thick succession of dark to light greenish gray (GLEY 1 4/10Y-7/10Y, GLEY 1 5GY series, and GLEY 1 10GY series) nannofossil-rich clay and clay with nannofossils (Figure F7). Clay makes up ~50%-70% of the sediment followed by calcareous nannofossils (10%-30%) (Figure F6). Increases in the proportions of glauconite (up to 7%) and siliceous sponge spicules (up to 4%) are observed. Bioturbation as indicated by burrows and mottled patches are observed throughout Unit III. Turbidites and ash layers are not present. Millimeter-scale dark greenish gray clasts are observed in the lower part of this unit (376.15–378.97 m CSF-A) (Figure F10A– **F10B**). At of the bottom of Unit III (378.97–379.11 m CSF-A) (Figure F10C), dark greenish gray pyrite and glauconite nodules ranging from millimeter to centimeter scale are present. The bottom of this unit is marked by a ~8 My hiatus during the Miocene (see Biostratigraphy). The Unit III/IV boundary is defined by changes in color and lithology and is characterized by a sharp and inclined contact

Figure F8. Photomicrographs of lithologic types, Site U1448. A. Nannofossilrich clay, Unit II. B. Clayey biosiliceous ooze, Unit IV. C. Volcanic ash, Subunit Ia. D. Volcanic ash including iron sulfides, Unit II. PPL = plane-polarized light.

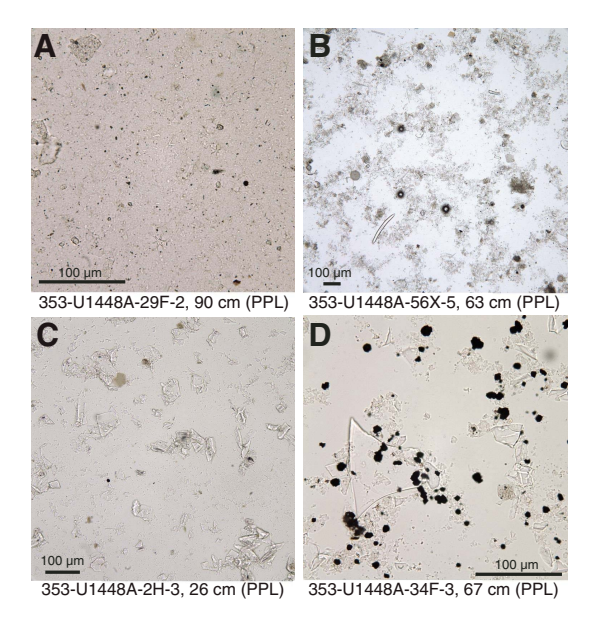


(Figure F10C). This lithostratigraphic boundary is also clearly visible in physical property data, illustrated by a subtle rise in magnetic susceptibility (MS) values, a sharp fall in NGR values (Figure F5), and concurrent changes in the gamma ray attenuation (GRA) and moisture and density (MAD) trends (see Physical properties). The hiatus boundary is characterized by bioturbation with smear slide and thin section observations showing burrows in Unit IV filled with nannofossil-rich clay from Unit III. Slight drilling disturbance is present in Unit III as biscuiting.

Unit IV

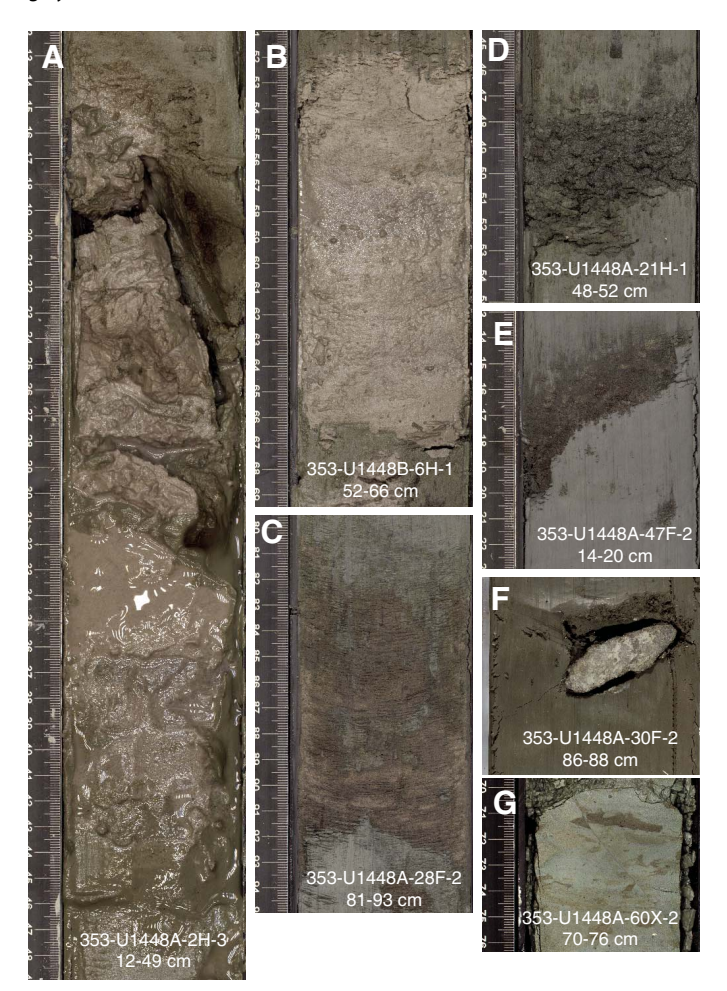
Interval: 353-U1448A-56X-5, 60 cm, through 60X-CC, 41 cm Depth: Hole U1448A = 379.11-420.60 m CSF-A

Age: early to middle Miocene

Major lithology: clayey biosiliceous ooze with nannofossils, clayey biosiliceous ooze, biosiliceous ooze with clay, and nannofossil-rich biosiliceous ooze with clay

Unit IV is a ~40 m thick succession of greenish gray to light greenish gray (GLEY 1 6/10Y-7/10GY and GLEY 1 5GY series) clayey biosiliceous ooze with nannofossils, clayey biosiliceous ooze, biosiliceous ooze with clay, and nannofossil-rich biosiliceous ooze with clay (Figures F7, F8). Smear slide observations indicate a substantial increase in biosilica and concurrent decrease in lithogenic grains relative to Unit III (Figure F6). Biosilica, dominated by diatoms, makes up ~40%-60% of the sediment, followed by clay (20%-40%), calcareous nannofossils (10%-30%), and glauconite (up to 15%) (Figure F6). Turbidites and ash layers are not present in Unit IV. The lithology of the uppermost ~30 cm interval of this unit (379.11–379.43 m CSF-A) shows light greenish gray (5G 7/1) clayey biosiliceous ooze and is characterized by abundant laminations (Figure F10D). In the underlying interval, the lithology gradationally changes to greenish gray (GLEY 1 6/10Y) biosiliceous ooze with varying proportions of clay and nannofossils. Bioturbation is present as indicated by burrows and mottled patches. Occasional laminations are visible and offset by microfaults (Figures F9G, F10E-F10F). Drilling disturbance is present as moderate to severe biscuiting.

Figure F9. Line-scan images of minor lithologies, Site U1448. A. Volcanic ash likely associated with the Toba eruption, Subunit Ia. B. Light gray volcanic ash, Subunit Ia. C. Pinkish gray volcanic ash, Unit II. D. Thin turbidite composed of black to dark gray bioclastic silt with foraminifers, Unit II. E. Very thin turbidite composed of greenish black bioclastic sand with silt, Unit II. F. Pyrite nodule, Unit II. G. Microfault offsetting mottled brown and greenish gray sediments, Unit IV.



Biostratigraphy

Calcareous nannofossils are abundant (50%–90% of sediment particles) throughout Hole U1448A, and their preservation is very good in the Pleistocene, Pliocene, and latest Miocene sediment sections (0–379.1 m CSF-A). A hiatus was observed at 379.11 m CSF-A, below which nannofossils are still abundant and moderately well preserved. The composition of assemblages allowed sediments between the hiatus and the bottom of Hole U1448A (420.6 m CSF-A) to be assigned a middle Miocene age. Foraminifers are well preserved in all core catcher samples from Hole U1448A. Foraminifers are dominant in the upper 340 m CSF-A. Abundance decreases to common just above the hiatus and drops to few to common below the hiatus. Diatoms are rarely present in the uppermost 379.04 m of Hole U1448A. They are abundant just below the hiatus, and their preservation varies from moderate to good.

The age model for Site U1448 was established by combining calcareous nannofossil, planktonic foraminifer, and diatom datums (the latter below the hiatus only). The oldest calcareous nannofossil

Figure F10. Line-scan images of Miocene hiatus interval near the Unit III/IV boundary, Hole U1448A. A. Nannofossil-rich clay, Unit III. B. Clay with nannofossils, Unit III. C. Inclined boundary between clay with nannofossils (Unit III) and clayey biosiliceous ooze (Unit IV). Dark green nodules containing glauconite and iron sulfides. Burrows in the upper few centimeters of Unit IV contain clay with nannofossils, similar to the lithology at the base of Unit III. D. Clayey biosiliceous ooze (Unit IV) with the Unit III/IV boundary, and the bottom few centimeters of clay with nannofossils (Unit III). E. Nannofossil-rich biosiliceous ooze, Unit IV. F. Clayey biosiliceous ooze with nannofossils, Unit IV.



sample studied above the hiatus (Sample 353-U1448A-56X-5W, 59 cm) contained both Discoaster quinqueramus and Reticulofenestra rotaria, suggesting an age between 5.94 and 6.91 Ma. The core catcher sample immediately below the hiatus (Sample 56X-CC) was older than 14.91 Ma based on calcareous nannofossils. Planktonic foraminifer datums suggest that the age of the oldest core catcher sample above the hiatus (Sample 55X-CC) is between 5.92 and 8.58 Ma and the age of the youngest core catcher sample below the hiatus (56X-CC) is older than 14.53 Ma. The oldest planktonic foraminifer datum encountered is the last occurrence (LO) of Praeorbulina glomerosa (14.78 Ma) in Sample 59X-CC. P. glomerosa is found in the deepest sample (60X-CC), defining the basal age of Hole U1448A as 14.78 to 16.27 Ma. The co-occurrence of the diatom species Rhaphidodiscus marylandicus and Annellus californicus in the lowermost part of Hole U1448A suggests that the bottom of Hole U1448A is older than 16.7 Ma (LO of R. marylandicus) and younger than 17.3 Ma (first occurrence [FO] of A. californicus).

Calcareous nannofossils

Calcareous nannofossils were examined in all core catcher samples from Hole U1448A. Additional split core samples from Hole U1448A were examined to refine the depth of biostratigraphic datums once they were defined between two core catcher samples. Semiquantitative species abundance estimates for all core catcher samples are shown in Table T2. Pleistocene to late Miocene nannofossil assemblages are typical of tropical/subtropical paleoenvironments and include common to abundant Florisphaera profunda, Gephyrocapsa spp., Reticulofenestra spp., Sphenolithus spp., Discoaster spp., Helicosphaera spp., Calcidiscus spp., and Umbilicosphaera spp. in Samples 353-U1448A-1H-CC through 56X-5W, 59 cm. Samples between 56X-5W, 61 cm, and 60X-CC contain common to abundant Helicosphaera spp., Sphenolithus heteromorphus, Discoaster spp., Coccolithus spp., and Umbilicosphaera spp. and few to common Cyclicargolithus floridanus. We were therefore able to construct a relatively high-resolution stratigraphy using nannofossils (Table T3; Figure F11). Reworked nannofossil specimens are few to rare (Table T2).

Pliocene-Pleistocene

Well to very well preserved calcareous nannofossils are present throughout the Pleistocene (0 to ~190 m CSF-A) and Pliocene (~190–330 m CSF-A) sedimentary section of Hole U1448A. All Pleistocene marker species defined by Martini (1971) and Okada and Bukry (1980) were found (Table T3) (see Biostratigraphy in the Expedition 353 methods chapter [Clemens et al., 2016a] for

Table T2. Semiquantitative calcareous nannofossils abundance counts from core catcher samples, Hole U1448A. **Download table in .csv format.**

zonal schemes used; all ages cited in the text and figures are those of Gradstein et al., 2012). *Emiliania huxleyi*, which delineates the base of Zone NN21 (0.29 Ma), is present in Sample 353-U1448A-3H-2W, 140 cm (14.8 m CSF-A), and all shallower samples studied based on shipboard scanning electron microscope work. The onset of dominance of *E. huxleyi* among the Noelaerhabdaceae could not be reliably determined because of the presence of various different small Noelaerhabdaceae species in the Late Pleistocene.

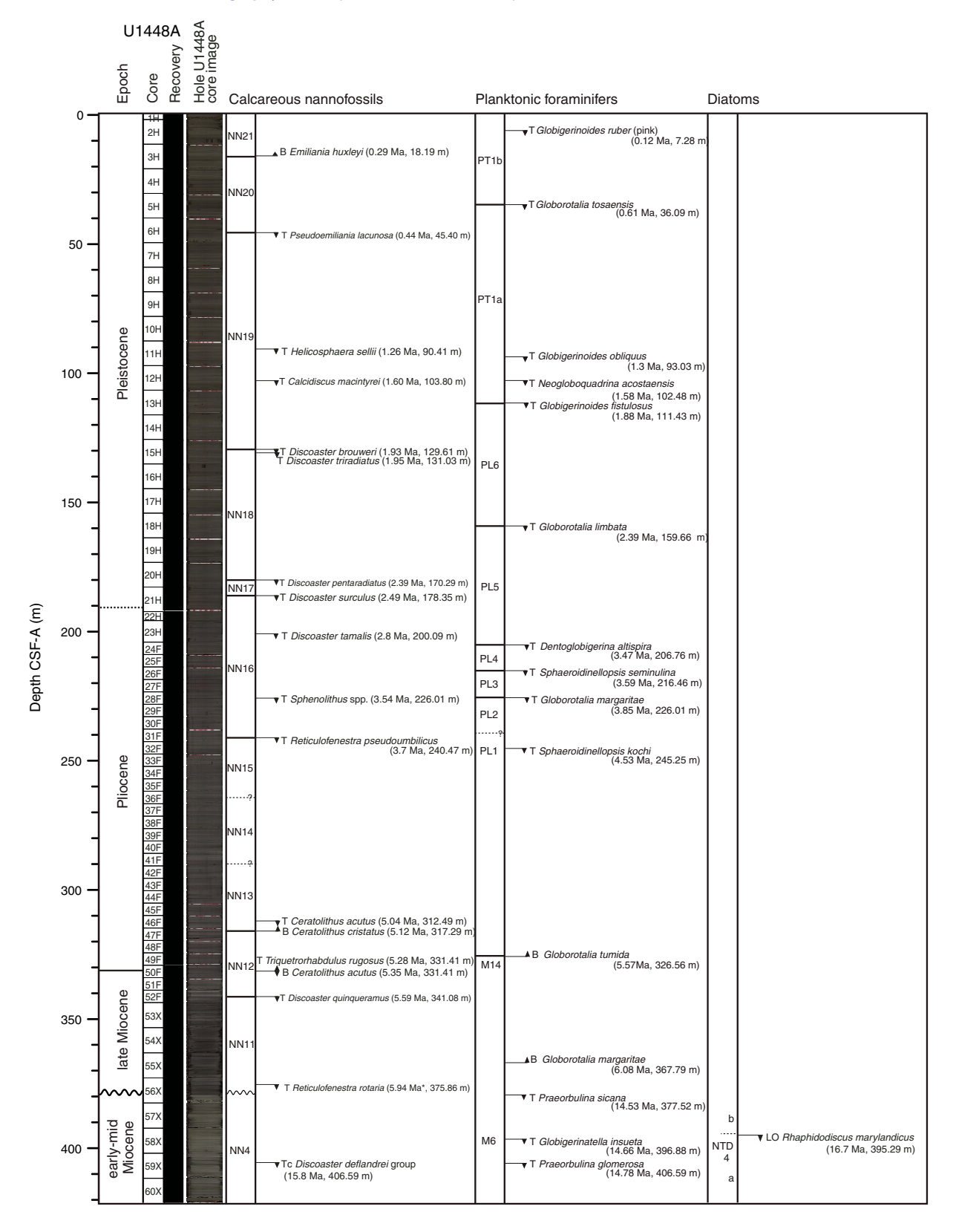
The LO of *Pseudoemiliania lacunosa*, dated at 0.44 Ma, occurs between Samples 353-U1448A-5H-CC and 6H-CC (midpoint depth = 45.40 m CSF-A). *Reticulofenestra asanoi* is present only in Sample 7H-CC. Large *Gephyrocapsa* (>5.5 µm) were of no biostratigraphic value at Site U1448 because of their rare and sporadic occurrences. Well-defined Pleistocene events at Site U1448 are the FOs of *Helicosphaera sellii, Calcidiscus macintyrei, Discoaster brouweri, Discoaster triradiatus, Discoaster pentaradiatus*, and *Discoaster surculus* (Table **T3**; Figure **F11**). We note that in Hole U1448A, *D. triradiatus* is rare where present; therefore, limited confidence can be placed in the exact depth of its LO at 1.95 Ma.

The Pliocene/Pleistocene boundary (2.59 Ma) is placed below the LO of *D. pentaradiatus* (2.39 Ma) between Samples 353-U1448A-19H-3W, 5 cm, and 19H-CC (midpoint depth = 170.29 m CSF-A) and above the LO of *Discoaster tamalis* (2.8 Ma) between Samples 22H-CC and 23H-CC. The LO of *Sphenolithus* species (3.54 Ma) occurs between Samples 27F-CC and 28F-CC (midpoint depth = 226.01 m CSF-A). *Reticulofenestra pseudoumbilicus* (>7 µm) was found in Sample 31F-CC (242.845 m CSF-A) and deeper. *Discoaster asymmetricus* was almost entirely absent from the Site U1448 assemblage. The LO of *Ceratolithus acutus* (5.04 Ma) occurs between Samples 45F-CC and 46F-CC (midpoint depth = 312.49 m CSF-A), whereas the FO of *Ceratolithus cristatus* (5.12 Ma, named

Table T3. Calcareous nannofossil datums, Hole U1448A. * = boundary age of Subzone NC9c, corresponding to Subzone NN11c in which the species occurs (Bown, 1998). B = bottom, T = top, Tc = top common, Ta = top acme. GTS2012 = Geologic Timescale 2012. **Download table in .csv format.**

					To	р			Bottom			Midpoint	
Species event	GTS2012 age (Ma)	Site	Hole	Core	Section	Interval (cm)	Depth CSF-A (m)	Core	Section	Interval (cm)	Depth CSF-A (m)	depth CSF-A (m)	Depth ± (m)
B Emiliania huxleyi	0.29	U1448	Α	3H	2W	140	14.80	3H	CC		21.57	18.19	3.39
T Pseudoemiliania lacunosa	0.44	U1448	Α	5H	CC		40.75	6H	CC		50.06	45.40	4.66
Tc Reticulofenestra asanoi	0.91	U1448	Α	6H	CC		50.06	7H	CC		59.76	54.91	4.85
T Helicosphaera sellii	1.26	U1448	Α	10H	CC		88.32	11H	4W	10	92.50	90.41	2.09
T Calcidiscus macintyrei	1.6	U1448	Α	12H	3W	5	100.38	12H	CC		107.22	103.80	3.42
T Discoaster brouweri	1.93	U1448	Α	14H	CC		126.46	15H	5W	120	132.76	129.61	3.15
T Discoaster triradiatus	1.95	U1448	Α	14H	CC		126.46	15H	CC		135.61	131.03	4.58
T Discoaster pentaradiatus	2.39	U1448	Α	19H	3W	5	166.96	19H	CC		173.62	170.29	3.33
T Discoaster surculus	2.49	U1448	Α	19H	CC		173.62	20H	CC		183.09	178.35	4.73
Pliocene/Pleistocene boundary	2.59												
T Discoaster tamalis	2.8	U1448	Α	22H	CC		195.90	23H	CC		204.29	200.09	4.19
T Sphenolithus spp.	3.54	U1448	Α	27F	CC		223.64	28F	CC		228.39	226.01	2.38
T Reticulofenestra pseudoumbilicus	3.7	U1448	Α	30F	CC		238.10	31F	CC		242.85	240.47	2.38
T Ceratolithus acutus	5.04	U1448	Α	45F	CC		310.06	46F	CC		314.92	312.49	2.43
B Ceratolithus cristatus	5.12	U1448	Α	46F	CC		314.92	47F	CC		319.67	317.29	2.38
T Triquetrorhabdulus rugosus	5.28	U1448	Α	50F	CC		324.25	51F	CC		338.58	331.41	7.16
Pliocene/Miocene boundary	5.33												
B Ceratolithus acutus	5.35	U1448	Α	50F	CC		324.25	51F	CC		338.58	331.41	7.16
T Discoaster quinqueramus	5.59	U1448	Α	51F	CC		338.58	52F	CC		343.58	341.08	2.50
T Reticulofenestra rotaria	5.94*	U1448	Α	55X	CC		372.62	56X	5W	59	379.10	375.86	3.24
Hiatus													
T Sphenolithus heteromorphus	13.53	U1448	Α	Hiatus				56X	CC		382.22		
T Helicosphaera ampliaperta	14.91	U1448	Α	Hiatus				56X	CC		382.22		
Ta <i>Discoaster deflandrei</i> group	15.8	U1448	Α	58X	CC		401.79	59X	CC		411.39	406.59	4.80
B Sphenolithus heteromorphus	17.71	U1448	Α	60X	CC		420.58	Below end of hole					

Figure F11. Summary of biostratigraphic events identified in Hole U1448A. T = top (last occurrence), B = bottom (first occurrence), Tc = top common. For biozonation schemes used, see **Biostratigraphy** in the Expedition 353 methods chapter (Clemens et al., 2016a).



Ceratolithus rugosus in Gradstein et al., 2012) occurs between Samples 46F-CC and 47F-CC (midpoint depth = 317.29 m CSF-A).

Miocene

The Miocene/Pliocene boundary (5.33 Ma) occurs between Samples 353-U1448A-50F-CC and 51F-CC (324.245 and 338.58 m CSF-A) based on the LO of Triquetrorhabdulus rugosus (5.28 Ma) and the FO of C. acutus (5.35 Ma) in this interval. The LO of D. quinqueramus (5.59 Ma) occurs between Samples 51F-CC and 52F-CC. A hiatus comprising the early late and late middle Miocene was observed in Sample 56X-5W, 60 cm, at 379.11 m CSF-A. R. rotaria, which occurs in Subzone CN9c/NN11c (Bown, 1998; 5.94-6.91 Ma based on the calibrated ages of Gradstein et al., 2012), was very rare in Sample 56X-3W, 50 cm, and rare in Sample 56X-5W, 59 cm (immediately above the hiatus); therefore, its LO can be placed just above the hiatus. This allows the oldest sediments recovered above the hiatus to be assigned to an interval between 5.94 and 6.91 Ma. Below the hiatus, all samples studied contained marker species S. heteromorphus (13.53-17.71 Ma) and Helicosphaera ampliaperta (>14.91 Ma). Discoaster deflandrei increased in abundance downcore from few to common between Samples 58X-CC and 59X-CC, and this likely represents the top common (Tc) D. deflandrei group event (15.8 Ma). No Discoaster signus (LO at 15.85 Ma) were unambiguously identified. Thus, we are able to constrain the age range of this middle-late Miocene section to 14.91-17.71 Ma based on nannofossils.

Planktonic foraminifers

Planktonic foraminifer biostratigraphy of the Pleistocene to Miocene section at Site U1448 was based on the shipboard study of core catcher samples from Hole U1448A with the addition of a single sample from Section 353-U1448A-13H-7, where a core catcher was not available. The distribution of planktonic foraminifers in Hole U1448A is shown in Table T4. The absolute ages assigned to

Table T4. Semiquantitative planktonic foraminifer abundance counts from core catcher samples, Hole U1448A. **Download table in .csv format.**

biostratigraphic datums listed in Table **T5** follow the references given in Table **T2** in the Expedition 353 methods chapter (Clemens et al., 2016a).

Planktonic foraminifer percentages are consistently high (mean = 93.9%) in the Pliocene–Pleistocene with total foraminifers averaging >17,000 per 10 cm³ of raw sediment. Planktonic foraminifer percentages are more variable in the Miocene, with the lowest value immediately above the hiatus. Total foraminifer numbers decrease dramatically beneath the hiatus. The planktonic/benthic ratio, reported as percentage planktonic foraminifers of the total foraminifer population, and the number of benthic foraminifers and total foraminifers found in a 10 cm³ sample are based on examination of the >150 μm size fraction of core catcher samples.

Pleistocene

Pleistocene planktonic foraminifer assemblages were recovered from Samples 353-U1448A-1H-CC through 23H-CC (2.43–204.30 m CSF-A). Foraminifers are dominant and very well preserved in all Pleistocene samples. Planktonic assemblages are dominated by the tropical to warm subtropical species *Globigerinoides ruber, Neogloboquadrina dutertrei, Globigerinoides sacculifer, Pulleniatina obliquiloculata*, and *Globigerinoides trilobus. Neogloboquadrina pachyderma* (dextral), *Orbulina universa, Globigerinita glutinata*, and *Globigerina bulloides* are significant and consistent contributors to the assemblage.

The LO of *G. ruber* (pink) in Sample 353-U1448A-2H-CC (12.12 m CSF-A) places these sediments in Zone PT1b. The top of Zone PT1a is located at the LO of *Globorotalia tosaensis* in Sample 5H-CC (40.75 m CSF-A). The LOs of *Globigerinoides obliquus* in Sample 11H-CC (97.75 m CSF-A), *Neogloboquadrina acostaensis* in Sample 12H-CC (107.22 m CSF-A), and *Globigerinoides fistulosus* in Sample 13H-7 (115.64 m CSF-A) define Zone PT1a. The LO of *Globorotalia limbata* in Sample 18H-CC (164.37 m CSF-A) is located in Zone PL5.

Pliocene

Pliocene planktonic foraminifer assemblages were recovered from Samples 353-U1448A-24H-CC through 48F-CC (209.23–

Table T5. Planktonic foraminifer datums, Hole U1448A. T = top, B = bottom. GTS2012 = Geologic Timescale 2012. Download table in .csv format.

Core	, section			GTS2012 age	De	(m)	Depth	
Тор	Bottom	Zone	Marker event	(Ma)	Тор	Bottom	Midpoint	
353-U1448A-	353-U1448A-							
1H-CC	2H-CC	PT1b	T Globigerinoides ruber (pink); Indo-Pacific	0.12	2.44	12.12	7.28	4.84
4H-CC	5H-CC	PT1b/PT1a	T Globorotalia tosaensis	0.61	31.44	40.75	36.10	4.66
10H-CC	11H-CC	PT1a	T Globigerinoides obliquus	1.30	88.32	97.75	93.04	4.72
11H-CC	12H-CC	PT1a	T Neogloboquadrina acostaensis	1.58	97.75	107.22	102.49	4.74
12H-CC	13H-CC	PT1a/PL6	T Globigerinoides fistulosus	1.88	107.22	115.64	111.43	4.21
17H-CC	18H-CC	PL6/PL5	T Globorotalia limbata	2.39	154.95	164.37	159.66	4.71
		Pleistocene/Pliocene boundary		2.59				
23F-CC	24F-CC	PL5/PL4	T Dentoglobigerina altispira (Pacific)	3.47	204.30	209.23	206.77	2.47
25F-CC	26F-CC	PL4/PL3	T Sphaeroidinellopsis seminulina (Pacific)	3.59	214.09	218.84	216.47	2.38
27F-CC	28F-CC	PL3/PL2	T Globorotalia margaritae	3.85	223.64	228.39	226.02	2.38
31F-CC	32F-CC	PL1	T Sphaeroidinellopsis kochi	4.53	242.85	247.66	245.26	2.41
		Pliocene/Miocene boundary		5.33				
48F-CC	49F-CC	PL1/M14	B Globorotalia tumida	5.57	324.58	328.54	326.56	1.98
54X-CC	55X-CC	M14	B Globorotalia margaritae	6.08	362.96	372.62	367.79	4.83
		Hiatus						
55X-CC	56X-CC	M6	T Praeorbulina sicana	14.53	372.62	382.22	377.42	4.80
57X-CC	58X-CC	M6	T Globigerinatella insueta	14.66	391.98	401.79	396.89	4.91
58X-CC	59X-CC	M6	T Praeorbulina glomerosa	14.78	401.79	411.39	406.59	4.80
60X-CC		M5a/M4b	B Praeorbulina sicana	16.27	420.58			

324.58 m CSF-A). Foraminifers are dominant and well preserved in all Pliocene samples. *G. sacculifer, Globigerinoides extremus, Dento-globigerina altispira, G. obliquus, G. trilobus,* and *N. dutertrei* dominate Pliocene samples. *G. ruber* does not appear in any sample deeper than 240 m CSF-A.

The LO of *D. altispira* in Sample 353-U1448A-24F-CC (208.23 m CSF-A) defines the upper boundary of Zone PL4. The LO of *Sphaeroidinellopsis seminulina* in Sample 26F-CC (218.84 m CSF-A) marks top of Zone PL3. The upper boundary of Zone PL2 is marked by the LO of *Globorotalia margaritae* in Sample 28F-CC (228.39 m CSF-A), and the LO of *Sphaeroidinellopsis kochi* in Sample 32F-CC (247.66 m CSF-A) marks the top of Zone PL1.

Miocene

Samples 353-U1448A-49F-CC through 60X-CC (328.54–420.58 m CSF-A) contain Miocene sediments. A hiatus exists between Samples 55X-CC and 56X-CC that may represent up to 8.6 My. Foraminifer abundance decreases with depth to common or few below the hiatus. Preservation is good throughout the Miocene. The planktonic foraminifer assemblage is dominated by *G. extremus, G. trilobus, D. altispira,* and *G. obliquus* above the hiatus, with consistent contributions from *G. sacculifer* and *Globoturborotalita woodi,* and contributions by *Globigerinoides subquadratus, Globigerinoides immaturus,* and *Praeorbulina sicana* below the hiatus.

The FO of *Globorotalia tumida* in Sample 353-U1448A-48F-CC (324.58 m CSF-A) identifies the top of Zone M14. The FO of *G. margaritae* in Sample 54X-CC (362.96 m CSF-A) identifies the samples immediately above the hiatus as falling within Zone M14. Below the hiatus, the LOs of *P. sicana* and *Globigerinatella insueta* in Samples 56X-CC (382.22 m CSF-A) and 58X-CC (401.79 m CSF-A), respectively, place these sediments in Zone M6. Zones M7–M13 are missing from the sedimentary record. *P. glomerosa* is found in Sample 60X-CC, suggesting that the basal age of Hole U1448A is between 14.78 and 16.27 Ma.

Diatoms

In order to define the sediment age and paleoenvironmental conditions, core catcher samples and samples from selected split core sections from Hole U1448A were investigated (Table **T6**). The

Table T6. Semiquantitative diatom abundance counts from core catcher and split core samples, Site U1448. **Download table in .csv format.**

sampling resolution deeper than Sample 353-U1448A-55X-CC was high, with the number of samples varying from 7 to 9 per core.

Diatom distribution in Hole U1448A is shown in Table **T6**. The absolute ages assigned to biostratigraphic datums listed in Table **T7** follow the references given in Table **T3** in the Expedition 353 methods chapter (Clemens et al., 2016a). Figure **F12** shows the age/depth of Site U1448 (also shown are nannofossils and foraminifer datums).

Diatom biostratigraphy

The prehiatus interval is characterized by many diatom species of common occurrence during the middle Miocene (*Coscinodiscus lewisianus, Cestodiscus pulchellus, Cestodiscus pulchellus* var. *maculatus, Cestodiscus robustus, Nitzschia maleinterpretaria, Thalassiosira fraga, A. californicus, Rossiella paleacea, Cestodiscus peplum, and R. marylandicus*). Among early and middle Miocene diatom bioevents (see Figure **F4B** in the Expedition 353 methods chapter [Clemens et al., 2016a]), only the LO of *R. marylandicus* (16.7 Ma) was well defined between Samples 353-U1448A-58X-5W, 81 cm, and 57X-CC. The presence of *T. fraga* at Sample 56X-CC suggests that the sediments below the hiatus are older than 16.1 Ma. Based on the occurrence of *A. californicus* at Sample 353-U1448A-58X-5W, 81 cm, the lowermost part of the Hole U1448A sediment column is younger than 17.3 Ma (see Figure **F4B** in the Expedition 353 methods chapter [Clemens et al., 2016a]).

Sedimentation rates and age model

Age-depth relationships for Hole U1448A based on biostratigraphy for the three fossil groups studied (calcareous nannofossils, planktonic foraminifers, and diatoms) show good agreement (Figure F12). The ages of nannofossil and planktonic foraminifer biostratigraphic events above and below the Miocene hiatus indicate a hiatus lasting ~8 My between 5.94–6.91 and 14.91–16.38 Ma (Figure F13).

Based on a linear fit including all data, sedimentation rates in Hole U1448A are around 5–6 cm/ky in the Pleistocene to late Miocene. A number of minor sedimentation rate changes can be identified in Figure F12; however, these changes cannot be reliably resolved until an orbital-resolution isotope stratigraphy has been generated. Below the hiatus, sedimentation rates in the early to middle Miocene sedimentary unit cannot be meaningfully resolved with the available biostratigraphic information from the three fossil groups at this time.

Table T7. Diatom datums, Site U1448. LO = last occurrence, FO = first occurrence, * = see the **Expedition 353 methods** chapter (Clemens et al., 2016a) for references. **Download table in .csv format.**

						-	Гор			Во	ttom		Midpoint	Interval
Co-occurring species/bioevent	Calibrated age* (Ma)	Age interval (Ma)	Site H	Hole	Core	Section	Interval (cm)	Depth CSF-A (m)	Core	Section	Interval (cm)	Depth CSF-A (m)	depth CSF-A (m)	depth CSF-A (m)
Thalassiosira fraga	LO 16.1-16.3	16.1–16.7	U1448	Α	56X	5W	62-62	379.13	57X	CC	0–5	391.98		379.13–391.98
Rhaphidodiscus marylandicus	LO 16.7		U1448	Α	57X	CC	0-5	391.98	58X	5W	81-81	398.63	395.31	
Annellus californicus	FO 17.3	16.7–17.3	U1448	Α	58X	5W	81–81	398.63	60X	CC	0–5	420.58		398.63-420.58

Figure F12. Biostratigraphic- and magnetostratigraphic-based age-depth plot, Hole U1448A. Vertical error bars show the depth range of the identified biostratigraphic events (e.g., between two core catchers or two core sections). Colored boxes show the upper and lower age constraints on the sedimentary unit below the hiatus for each fossil group. Color shading shows the ages of the Pleistocene, Pliocene and Miocene.

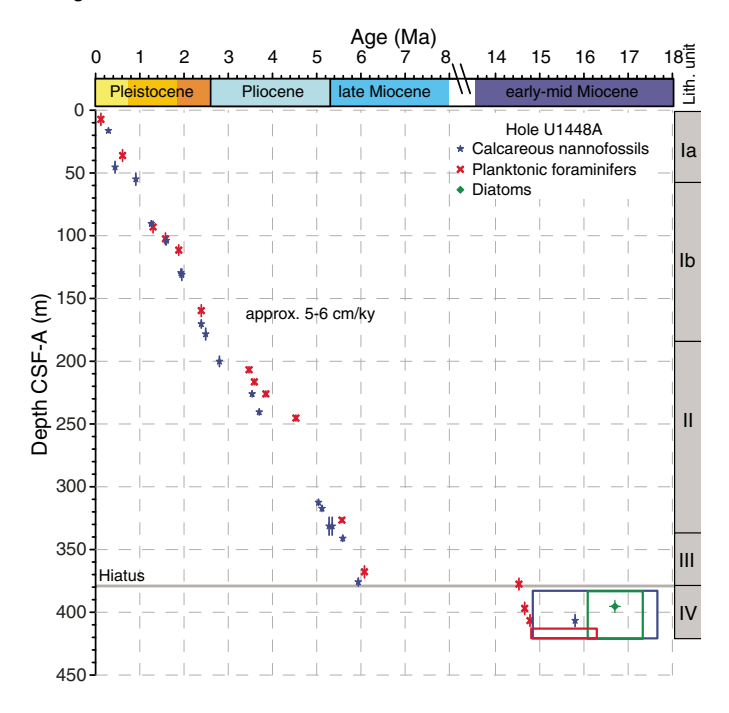
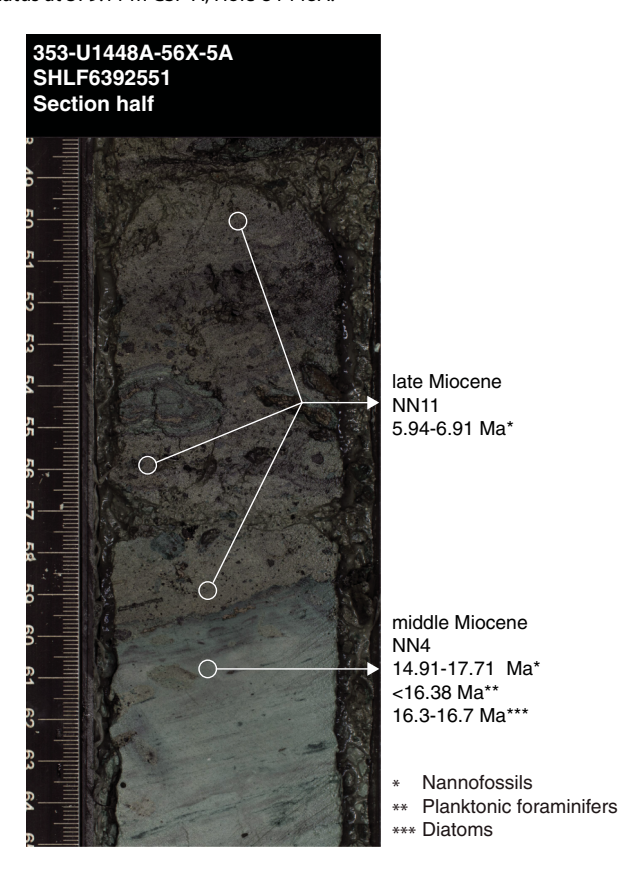


Figure F13. Biostratigraphic ages of several horizons above and below the hiatus at 379.11 m CSF-A, Hole U1448A.



Geochemistry

The geochemistry of Site U1448 mainly reflects the anaerobic processes of sulfate reduction and methanogenesis associated with microbial degradation of organic matter. The organic carbon content ranges from 0.2 to 1.4 wt% and clearly shows two zones: one with a mean value of ~1 wt% and another with ~0.4 wt%. The transition in organic carbon content occurs at ~200 m CSF-A (lithostratigraphic Subunit Ib/Unit II boundary). Headspace methane concentration increases immediately below the sulfate depletion zone and continues downcore with the highest values between 200 and 250 m CSF-A. The overall concentrations, however, are quite low (<30 parts per million [ppm]) compared to nearby Site U1447. Pore water sulfate decreases from 28 mM at the sediment/water interface to nearly zero at approximately 40 m CSF-A. Alkalinity has a broad peak, significantly lower than at Site U1447, from 40 to 150 m CSF-A before gradually decreasing, consistent with the production of bicarbonate during sulfate reduction. A monotonic increase in dissolved Ba concentration with depth suggests ongoing barite dissolution. Changes in the concentration of other elements and ions (Fe, Mn, Ca, B, ammonia, and Sr) in interstitial water can be readily explained by microbially mediated chemical reactions and their effects on pH, alkalinity, and mineral dissolution and precipitation. Sedimentary carbonate content varies significantly between 12 and 37 wt%.

Sediment gas sampling and analysis

Headspace gas samples were taken at a frequency of one sample per core in Hole U1448A as part of the routine environmental protection and safety-monitoring program (Table $\bf T8$). Methane concentration increases from 2 ppm between 0 and 49 m CSF-A to values of 13–28 ppm in three peaks at 97, 203, and 237 m CSF-A, before decreasing to <5 ppm from 290 m CSF-A until the bottom of the hole (Figure $\bf F14$). Heavier hydrocarbons such as ethane and propane were not detected.

Bulk sediment geochemistry

Calcium carbonate, inorganic carbon, and total organic carbon (TOC) contents were determined on sediment samples from Hole U1448A (Table **T9**; Figure **F15**). CaCO $_3$ content ranges between 12 and 37 wt% and is generally lower in the lower part of Subunit Ib and upper part of Unit II. TOC ranges between 0.2 and 1.4 wt% and clearly shows two zones: one with mean value of ~1% and another with ~0.4%. The transition between these TOC content zones occurs at ~200 m CSF-A (the lithostratigraphic Subunit Ib/Unit II boundary).

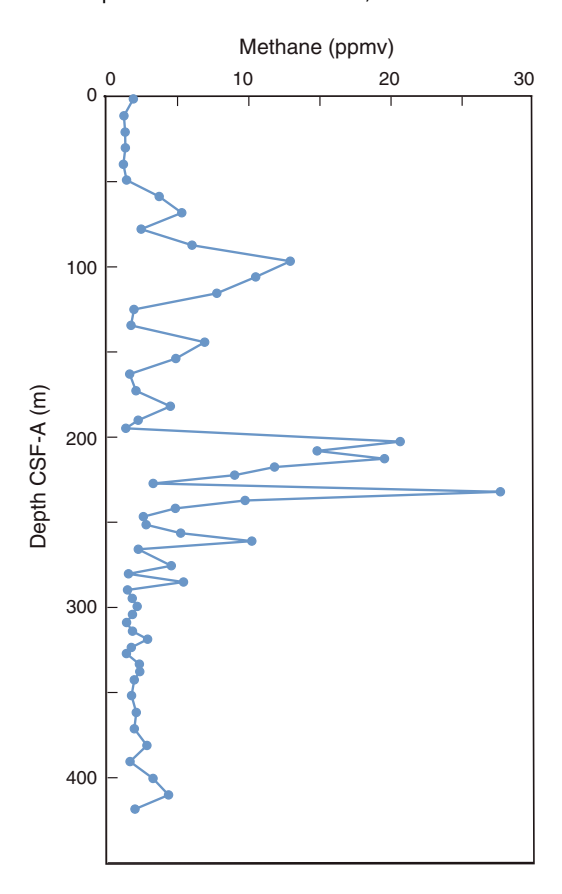
Interstitial water sampling and chemistry

Hole U1448A was sampled for pore water chemistry at a relatively coarse resolution of one sample per core for the uppermost section, switching to every other core for HLAPC and XCB cores. The whole-round samples for pore water squeezing were kept under N_2 during extraction of interstitial waters.

Concomitant with a sharp drawdown of sulfate in the uppermost 40 m, an increase in alkalinity is observed (Figure **F16**; Table **T10**). Although sulfate is below detection from ~40 m CSF-A to the base of the hole, Ba increases sharply from a few micromolar at ~11 m CSF-A to ~72 μ M at ~49 m CSF-A. Alkalinity peaks at ~15 mM

Table T8. Headspace methane concentrations, Hole U1448A. **Download** table in .csv format.

Figure F14. Headspace methane concentrations, Hole U1448A.



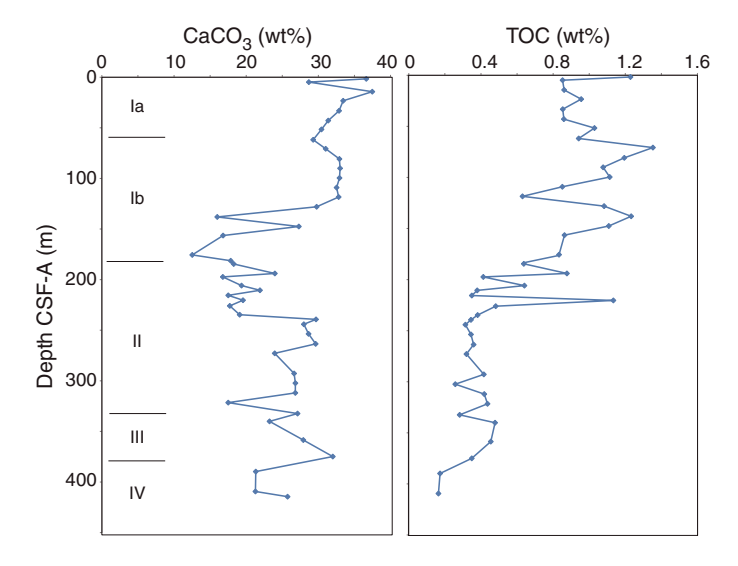
at 40 m CSF-A and has a broad peak to 150 m CSF-A before gradually decreasing to ~9.7 mM at 241 m CSF-A, consistent with the production of bicarbonate during sulfate reduction. Alkalinity is lower than at Site U1447. Ammonium increases from 0.2 mM in the top of Hole U1448A to 3.5 mM at 135 m CSF-A in Hole U1448A, before decreasing gradually downhole to values of ~1.5 mM.

Calcium concentration decreases from around 10 mM near the sediment/water interface to \sim 3.4 mM at \sim 40 m CSF-A then increases gradually with depth (Figure F16). The drop in Ca concentration in the top 40 m CSF-A is probably related to production of bicarbonate with sulfate reduction. Magnesium concentration is highest at the sediment/water interface, gradually decreases to a minimum of \sim 38 mM around 125 m CSF-A, and remains more or less constant until 222 m CSF-A. Deeper than 222 m CSF-A, Mg

Table T9. Calcium carbonate and carbon contents, Hole U1448A. **Download table in .csv format.**

Table T10. Interstitial water chemistry, Hole U1448A. **Download table in .csv format.**

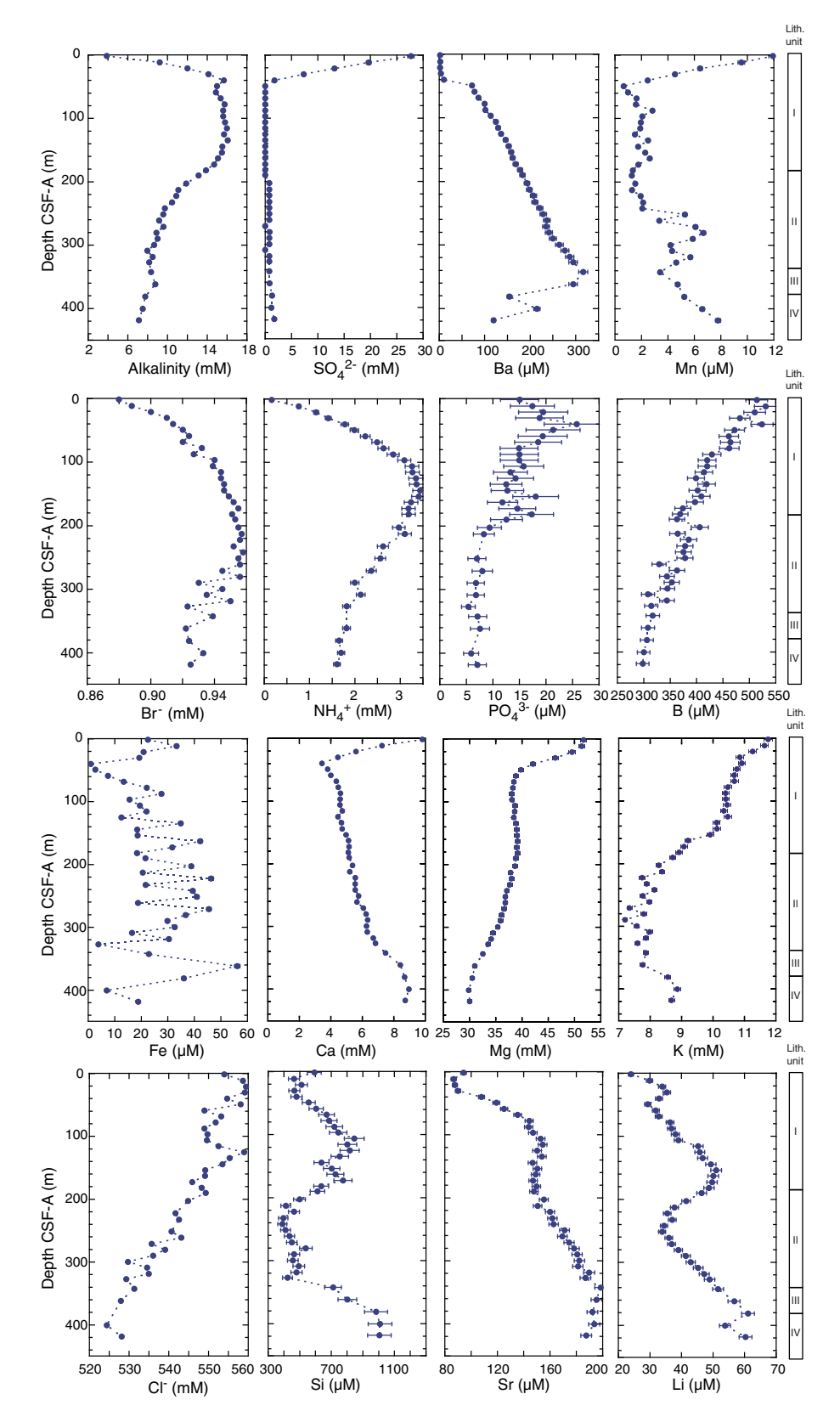
Figure F15. Calcium carbonate and TOC contents, Hole U1448A.



again decreases gradually to around 29 mM until the bottom of the hole. Lithium, Si, and Sr all show similar downhole concentration patterns with peaks around 140 m CSF-A, followed by a trough and increase to a peak deeper than 380 m CSF-A. The minimum and maximum concentrations of Li, Sr, and Si are 24, 94, and 464 and 60, 187, and $1009 \,\mu\text{M}$, respectively (Figure **F16**; Table **T10**).

Dissolved Mn concentration decreases rapidly from 12 to 0.67 μM in the uppermost 49 m, consistent with microbial reduction of Mn oxides in the uppermost sediments. (Figure **F16**; Table **T10**). Dissolved Fe concentration decreases from 33 to $\sim\!0.96~\mu M$ within the top 40 m CSF-A of the sediment column, possibly associated with sulfate reduction and the production of hydrogen sulfide scavenging soluble Fe. Below this minimum, dissolved Fe varies between $\sim\!2$ and 57 μM in the remaining sediment column, probably reflecting variable amounts and dissolution of residual iron oxides in sediments. Boron concentration decreases in a stepwise manner from around 514 μM at 0 m CSF-A to 298 μM at the bottom of the sedimentary section.

Figure F16. Pore water alkalinity, SO_4^{2-} , Ba, Mn, Br⁻, NH_4^+ , PO_4^{3-} , B, Fe, Ca, Mg, K, Cl⁻, Si, Sr, and Li, Hole U1448A. Error bars represent two standard deviations of repeated measurements of IAPSO seawater or a pore water sample (see **Geochemistry** and Tables **T5** and **T6**, all in the Expedition 353 methods chapter [Clemens et al., 2016a]).



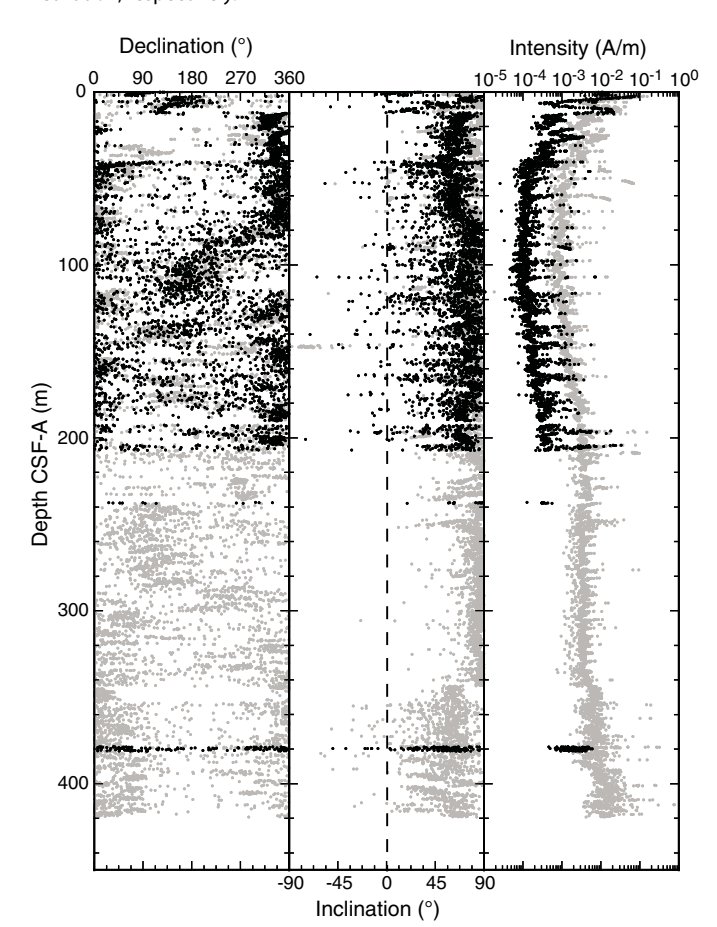
Paleomagnetism

Paleomagnetic measurements were conducted on archive-half sections for all three holes at Site U1448 (Figures F17, F18). To accommodate the core flow, only APC and HLAPC cores from Hole U1448A were demagnetized by an alternating field (AF) up to 10 mT. XCB cores from Hole U1448A and APC cores from Holes U1448B and U1448C were measured predominantly for natural remanent magnetization (NRM), with a few exceptions. HLAPC cores from Hole U1448B were not measured because of time constraints. Discrete samples taken from the working-half sections of Hole U1448A (N = 90) were also analyzed, with stepwise AF demagnetization typically up to 80 mT. Generally, the determination of characteristic remanence was difficult (Table T11). The stability of NRM appears to be higher just below the hiatus at 379.11 m CSF-A, with possible polarity transitions recorded. Anhysteretic remanent magnetization (ARM) was acquired and measured on a selection of discrete samples from Hole U1448A for preliminary insight into depth variations in Site U1448 sediment bulk magnetic properties.

Magnetostratigraphy

Cores 353-U1448A-3H through 23H and 353-U1448B-3H through 19H were oriented using the Icefield MI-5 tool. Therefore, we have obtained "true" declinations between 3.30 and 260.20 for Hole U1448A and between 18.40 and 133.45 m CSF-A for Hole

Figure F17. Downhole variations in declination, inclination, and intensity, Hole U1448A. Gray and black symbols = before and after 10 mT AF demagnetization, respectively.



U1448B (Figures **F17**, **F18**; Table **T12**). The true declinations generally concentrate around 0 (360°) or 180° downhole to ~200 m CSF-A for both holes. Inclinations of both NRM and NRM after 10 mT demagnetization were steep downward (near 90°), indicating severe drilling-related overprint. Discrete samples also revealed severe drilling-related overprint, except for samples shallower than 2.1 m CSF-A.

The true declinations from archive halves suggest that both Hole U1448A and U1448B sediments downhole to ~200 m CSF-A can be largely divided into three magnetozones (Figure F19). The biostratigraphic results (see Biostratigraphy) indicate that the Pliocene/Pleistocene boundary (2.58 Ma) corresponds to ~170 m CSF-A. On this basis, we speculate that the three magnetozones correspond to Brunhes (C1n), Matuyama (C1r), and Gauss (C2An) Chrons. However, scatter in the declination data prevents further refinement of magnetostratigraphy.

Bulk magnetic properties

ARM (0.05 mT direct current field, 80 mT AF field) was acquired on a selection of discrete samples taken from the working halves of Hole U1448A. ARM broadly measures relative changes in the concentration of ferrimagnetic minerals, where increases in the concentration of finer grained particles will increase ARM values much greater than an equivalent change in coarser grained particles. A significant decrease in ARM values for Hole U1448A at 10 m CSF-A (Figure F20) suggests either a decrease in the input, or the

Figure F18. Downhole variations in declination, inclination, and intensity, Hole U1448B.

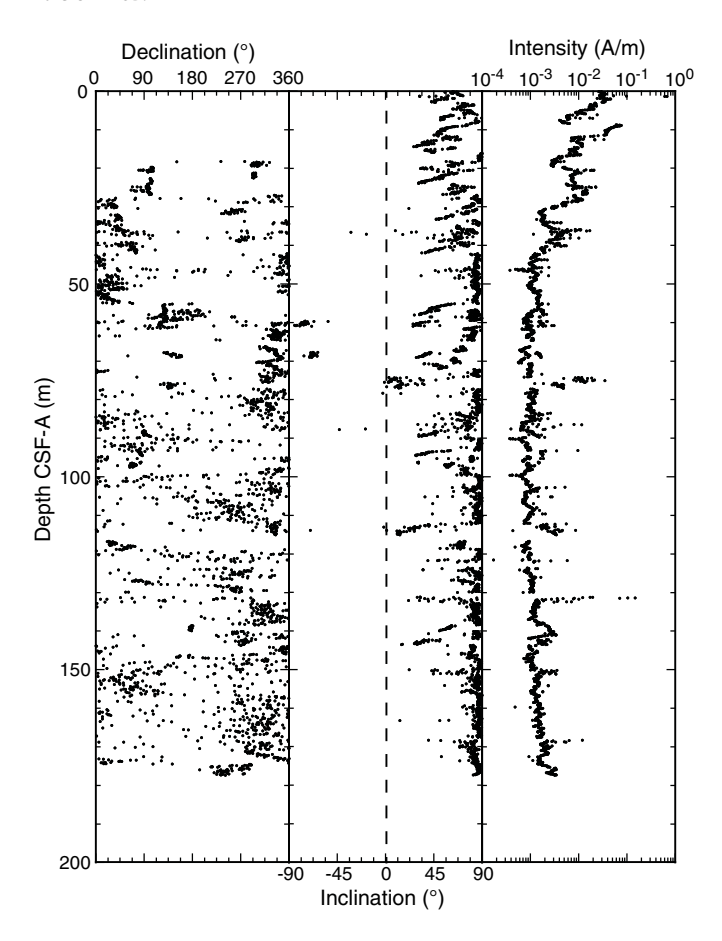


Table T11. Summary of discrete sample measurements, Hole U1448A. NRM = natural remanent magnetization, PCA = principal component analysis, MAD = maximum angular deviation. (Continued on next page.) **Download table in .csv format.**

Hole	Core	Туре	Section	Offset (cm)	Depth CSF-A (m)	Mass (g)	NRM (A/m)	PCA declination (°)	PCA true declination (°)	PCA inclination (°)	MAD (°)	MAD (°)	PCA anchored	PCA start (mT)	PCA end (mT)
A	1	Н	1	70	0.7	12.886	0.0218	151	82	-3.8	31.8	1.4	Υ	10	80
Α	1	Н	2	56	2.06	13.17	0.02759	129.8	60.8	13.3	14.9	3.3	Υ	10	80
Α	2	Н	2	75	4.65	13.532	0.007184								
Α	2	Н	4	80	7.7	13.683	0.002575								
Α	3	Н	3	70	15.6	13.106	0.003269								
Α	3	Н	5	30	18.2	14.133	0.00489								
Α	4	Н	2	90	23.8	14.14	0.00268								
A	4	H	6	56	29.42	14.301	0.002083								
A	5	Н	2	70	33.1	14.589	0.001252								
A A	5 6	H H	6 2	80 80	39.13 42.7	14.296 14.648	0.001429 0.0008122								
A	6	Н	4	55	45.22	14.44	0.0008122	273.9	248.9	4.6	16.7	1.7	Υ	10	40
A	6	н	6	75	48.43	14.663	0.001978	273.9	240.9	4.0	10.7	1.7		10	40
A	7	н	2	70	52.1	14.659	0.0008627								
Α	7	Н	6	80	58.2	14.494	0.0000027								
Α	8	Н	2	80	61.7	14.894	0.0007277	123.3	14.3	12	21.9	7.4	Υ	5	80
Α	8	Н	6	80	67.65	14.711									
Α	9	Н	2	70	71.1	14.686	0.000769								
Α	9	Н	6	80	77.2	14.788									
Α	10	Н	2	70	80.6	14.774	0.0006407								
Α	10	Н	6	85	86.75	14.463	0.0007111								
Α	11	Н	2	75	90.15	14.89	0.0005953								
Α	11	Н	6	75	96.15	14.761	0.000674								
Α	12	Н	2	74	99.65	14.755	0.0005843								
A	12	H	6	74	105.32	14.68	0.0006975								
A	13	Н	2	74	109.15	14.953	0.0005619								
A A	13 14	H H	6 2	74 74	114.85 118.56	14.63 15.021	0.0006298								
A	14	Н	6	74 74	124.31	14.717	0.0006298								
A	15	н	2	74	124.51	15.006	0.000842								
A	15	н	6	74	133.72	15.289	0.001031								
Α	16	Н	2	115	138.06	15.112	0.0008533								
Α	16	Н	6	58	143.39	15.166	0.0009806								
Α	17	Н	2	112	147.53	15.074	0.0007223								
Α	17	Н	4	88	150.35	15.304	0.0007608								
Α	18	Н	2	73	156.55	15.224	0.001036								
Α	18	Н	6	73	162.31	15.373	0.001194								
Α	19	Н	4	100	169.42	15.368	0.001174								
Α	19	Н	6	74	172.04	15.484									
Α	20	Н	1	73	174.13	15.36									
Α	20	Н	4	73	178.36	15.756	0.001964								
A	21	Н	2	72	185	15.461	0.001022	04.4	0.4	10.6	20.4	. .		10	
A	21	Н	4	105	188.3	15.609	0.001822	94.4	8.4	18.6	20.4	5.6	Υ	10	60
A A	22 23	H H	2 2	50 55	194.31 197.62	15.101 15.42	0.001976 0.002539								
A	23	Н	6	60	203.38	15.761	0.002339								
A	24	F	2	75	206.46	14.48	0.002148								
A	25	F	2	75	211.16	15.536	0.002110								
Α	26	F	2	90	216.12	15.361	0.002232								
Α	27	F	2	80	220.81	15.109	0.001926	137.7	137.7	-2.6	29.1	5.6	Υ	40	80
Α	28	F	2	60	225.5	15.356	0.002482								
Α	29	F	2	60	230.2	15.057	0.003015	122.5	122.5	16.9	22.8	4.6	Υ	10	80
Α	30	F	2	50	234.91	15.349	0.002786								
Α	31	F	2	60	239.7	14.41	0.002186								
Α	32	F	2	80	244.75	14.642	0.001735								
Α	33	F	2	65	249.46	15.238	0.001988								
Α	34	F	2	40	254	14.943	0.001601								
Α	35	F	2	85	259.26	14.593	0.002284								
A	36	F	2	90	264.1	13.456	0.00183								
A	37	F	2	90	268.9	13.845	0.001745								
A	38	F	2	80	273.57	14.251	0.002005								
A	39 40	F	2	80	278.4	15.074	0.001754								
A	40 41	F	2	90 60	283.25	14.772	0.002362								
A	41 42	F F	2 2	60 73	287.8	14.429 15.096	0.002457								
A A	42	F	2	73 73	292.73 297.53	15.096 15.16	0.002207 0.002301								
	43 44	F	2	73 73											
Α	44	F	2	/3	302.43	15.23	0.002352								

Table T11 (continued).

Hole	Core	Туре	Section	Offset (cm)	Depth CSF-A (m)	Mass (g)	NRM (A/m)	PCA declination (°)	PCA true declination (°)	PCA inclination (°)	MAD (°)	MAD (°)	PCA anchored	PCA start (mT)	PCA end (mT)
Α	45	F	2	73	307.22	14.546	0.002071								
Α	46	F	2	74	312.02	14.663	0.002185								
Α	47	F	2	74	316.76	11.66	0.001479								
Α	48	F	2	74	321.6	15.132	0.002087								
Α	49	F	2	74	326.39	14.613	0.00215								
Α	50	F	2	87	331.37	14.441	0.002041								
Α	51	F	2	31	335.21	13.327	0.002373								
Α	52	F	2	97	340.83	13.183	0.002677								
Α	53	Χ	4	68	348.59	14.015	0.001485								
Α	54	Χ	4	102	358.62	12.531									
Α	55	Χ	4	67	367.98	13.462									
Α	56	Χ	2	94	374.95	15.195	0.004649								
Α	56	Χ	4	86	377.87	14.566	0.003713								
Α	56	Χ	5	118	379.69	11.989	0.002569	297.2	297.2	-25.1	19.8	4.1	Υ	10	80
Α	56	Χ	6	38	380.4	11.536	0.002529								
Α	57	Χ	2	87	384.57	12.651	0.001653								
Α	57	Χ	7	50	391.12	11.362	0.002305	215.3	215.3	39.2	24.7	10.4	Υ	10	60
Α	58	Χ	3	90	395.75	11.991	0.003691	206.2	206.2	48.9	32	4.2	Υ	10	30
Α	58	Χ	5	108	398.9	12.205	0.004395	149.9	149.9	57.4	29.4	4.4	Υ	10	30
Α	59	Χ	2	80	403.9	12.656	0.003482								
Α	59	Χ	4	125	407.35	10.94	0.003341								
Α	60	Χ	2	48	412.84	11.7	0.003015	117.1	117.1	59.4	8.5	7.1	Υ	10	60
Α	60	Χ	5	70	416.62	11.91	0.005281								

Table T12. Magnetic toolface (MTF) values obtained from the Icefield MI-5 tool/FlexIT tool, Site U1448. **Download table in .csv format.**

	Н	ole U1448A	Hol	e U1448B
Core	MTF	Comment	MTF	Comment
1H	291	Unofficial	_	
2H	157	Unofficial	_	
3H	81.0		17.3	
4H	93.0	Range 88-98	317.6	
5H	358.0		348.4	
6H	335.0	Range 200-340	277.5	
7H	261.0		214.1	
8H	251.0		242.5	
9H	277.0		228.2	
10H	112.0		15.0	
11H	121.0		359.6	
12H	111.0		260.5	
13H	325.0		242.7	
14H	255.0		170.5	
15H	227.0		259.9	
16H	16.0		2.7	
17H	265.0		172.2	
18H	266.0		42.7	
19H	234.0		222.2	
20H	94.0		_	
21H	274.0		_	
22H	69.0		_	
23H	275.0		_	

removal, of fine-grained ferrimagnetic minerals. This is likely a response to early diagenesis (see **Geochemistry**). The decrease at this depth (10 m CSF-A) is similar to what we see at IODP Site U1445 in

the Mahanadi basin (see **Paleomagnetism** in the Site U1445 chapter [Clemens et al., 2016b]) and at Site U1447 in the Andaman Sea (see **Paleomagnetism** in the Site U1447 chapter [Clemens et al., 2016c]). Outside of the noticeable low in ARM observed between 205 and 215 m CSF-A, there is a steady increase in ARM with depth. In addition, ARM increases significantly below the hiatus at ~379 m CSF-A. Interpretations for these variations are currently unknown and further rock magnetic measurements in parallel with other proxies are required.

Magnetic signal around hiatus

Discrete Sample 353-U1448A-56X-5W, 118-120 cm (379.7 m CSF-A), shows a much higher stability of NRM against AF demagnetization than other discrete samples measured near the hiatus in Hole U1448A (Figure F21). This sample comes from ~60 cm below the inferred hiatus (see Lithostratigraphy). To investigate the spatial distribution of this anomalous signal, Section 56X-5A was measured at a 2 cm resolution with demagnetization steps of 5 and 10 mT. NRM intensity shows a clear peak at 19-29 cm offset of this section. Interestingly, this peak disappeared upon AF demagnetization, and the ratio of NRM intensity after 10 mT demagnetization to the NRM intensity shows two peaks at 105 and 127 cm offset (Figure F22). In addition, when plotting directional changes, the measurements around the shallower peak suggest a negative inclination similar to discrete Sample 56X-5W, 118-120 cm, whereas measurements around the deeper peak show endpoint directions antiparallel to that. We speculate that these signals indicate polarity transitions across these two peaks.

Figure F19. Speculative magnetostratigraphy, Holes U1448A and U1448B. Dashed blue lines = transitions in declination values. The unreliable intervals (orange bands) are largely caused by flux jumps in the *y*-axis superconducting quantum interference device.

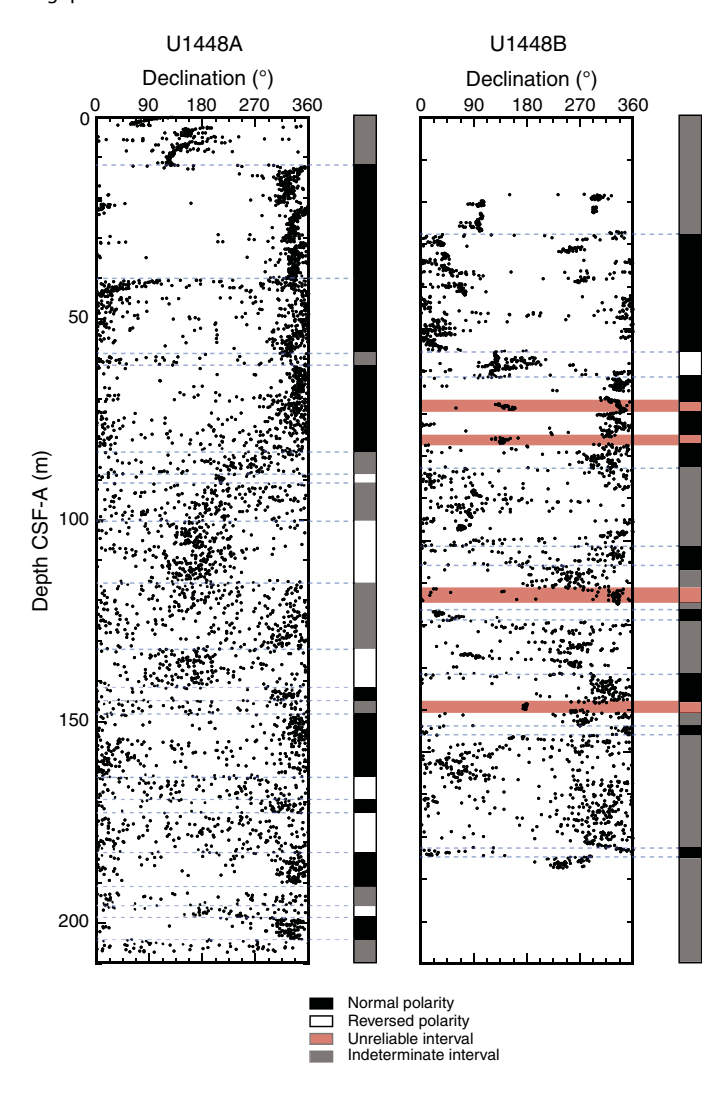


Figure F20. Downhole variations in mass-normalized ARM acquired on Hole U1448A discrete samples.

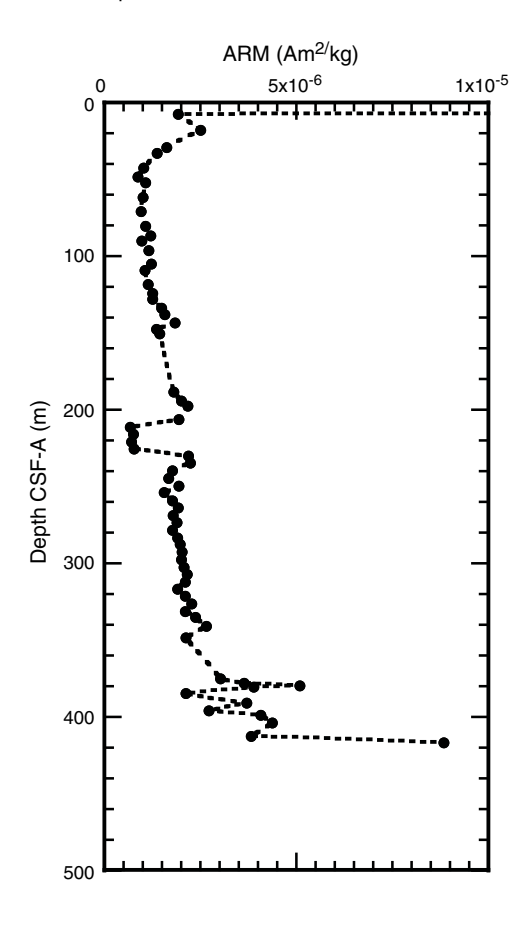


Figure F21. Stepwise demagnetization results for discrete Sample 353-U1448A-56X-5W, $118-120\ cm$.

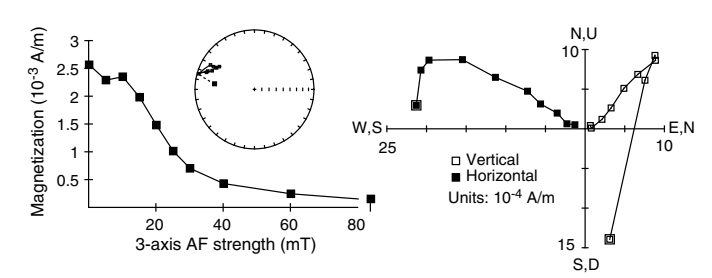
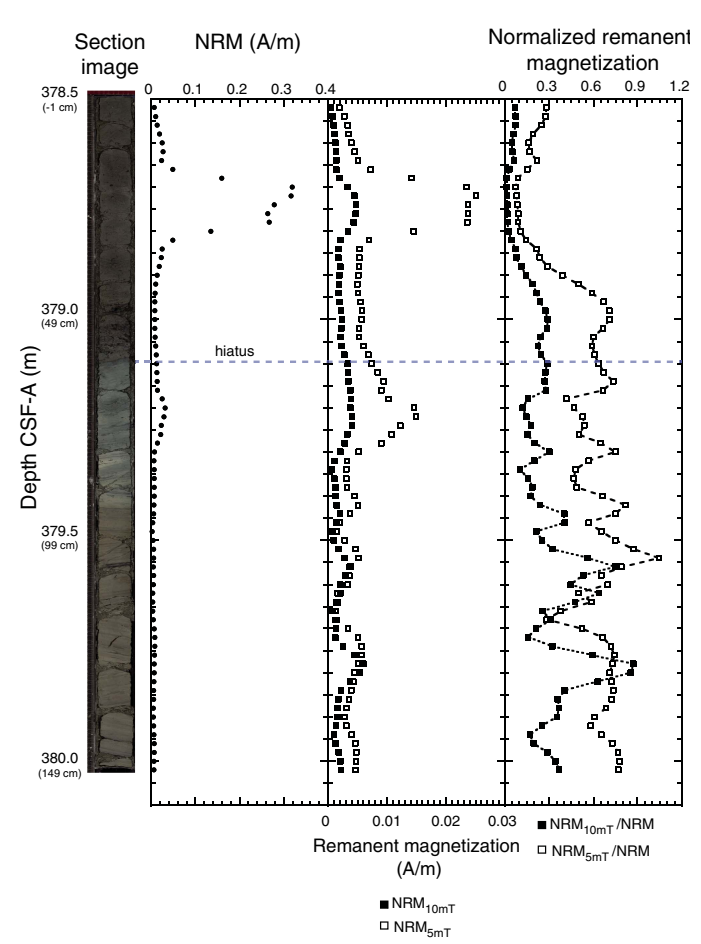


Figure F22. High-resolution (2 cm) section measurements across the hiatus (~379.2 m CSF-A), showing NRM, NRM after 5 and 10 mT AF demagnetization, and NRM after demagnetization normalized by the original NRM.



Physical properties

Standard physical property measurements were collected in Holes U1448A–U1448C. For Hole U1448A (0–440.6 m CSF-A), we defined six physical property (PP) units based on significant changes within the physical property measurements (Table T13): Units 1 (0–30.9 m CSF-A), 2 (30.9–107.2 m CSF-A), and 3 (107.2–182.9 m CSF-A) are independent of the lithostratigraphic units, and Units 4 (182.9–338.6 m CSF-A), 5 (338.6–379.1 m CSF-A), and 6 (379.1–440.6 m CSF-A) correspond to lithostratigraphic Units II, III, and IV, respectively (see Lithostratigraphy). Hole U1448B (0–358.22 m CSF-A) is generally in good agreement with Hole U1448A. This report predominantly discusses Hole U1448A. Hole U1448C was a geochemistry hole and therefore is not being discussed here

GRA, MS, P-wave velocity (V_p), and NGR measurements were acquired on all whole-round sections using the Special Task Multisensor Logger (STMSL), the Whole-Round Multisensor Logger (WRMSL), and the Natural Gamma Radiation Logger (NGRL). Whole-round sections from Hole U1448A were logged on the STMSL and then the WRMSL at a 10 cm sampling resolution before being taken to the core rack for thermal equilibration to ~18°C. The WRMSL was used to provide measurements for stratigraphic correlation purposes, and all sections from Holes U1448B and U1448C were logged for GRA and MS data using the WRMSL only at a 10–

Table T13. Physical property units, Site U1448. **Download table in .csv format.**

Unit	Depth CSF-A (m)
1	0-30.9
2	30.9-107.2
3	107.2-182.9
4	182.9-338.6
5	338.6-379.1
6	379.1-440.6

15 cm sampling interval. Following thermal equilibration, sections were logged on the NGRL. Sediment samples were collected from the working halves of Sections 2, 4, and 6 for MAD analyses. The archive-half sections were used to collect color reflectance and point MS data on the Section Half Multisensor Logger (SHMSL) and red, green, and blue (RGB) data on the Section Half Imaging Logger (SHIL). The data plots presented here (Figures F23, F24, F25, F26, F27, F28, F29, F30, F31, F32) were filtered to remove outliers from endcaps, voids, and foam spacers. We present the minimum, maximum, and mean values of all measured parameters for downhole and hole-to-hole comparison (Table T14). No infrared thermal anomalies were detected at this site.

Magnetic susceptibility

The STMSL and WRMSL MS values recorded for Hole U1448A show minor variability overall, with values between 1.28 and 37.61 instrument units (IU) (Figure F23). PP Unit 1 is characterized by higher average MS values with high variability possibly related to the unconsolidated nature of these upper sediments. PP Unit 2 remains relatively constant with an average value of 7.69 IU. PP Unit 3 is characterized by little variability but a steady increase from ~7.66 to 12.26 IU downhole to PP Unit 4. There is more variability in PP Unit 4 than in PP Units 2 or 3 with values ranging between 2 and 21.79 IU. PP Unit 5 has little variability with an average value of 10.9 IU, and there is a sharp drop in MS between PP Units 5 and 6 that was determined to be an ~8 Ma hiatus (see Biostratigraphy) (Figure F23). The STMSL and WRMSL track measurements agree nicely with the SHMSL point measurements trends; however, there is a constant offset between the whole-round and point measurements. It is likely that the slight increase in MS values downhole is related to compaction, whereas the generally low variability suggests no significant changes to the lithogenic flux or dilution to the lithogenic fraction from an increase in carbonate content on longterm geologic timescales between PP Units 1 and 5. PP Unit 6, however, does show a dramatic drop in MS, GRA, and NGR measurements following the hiatus.

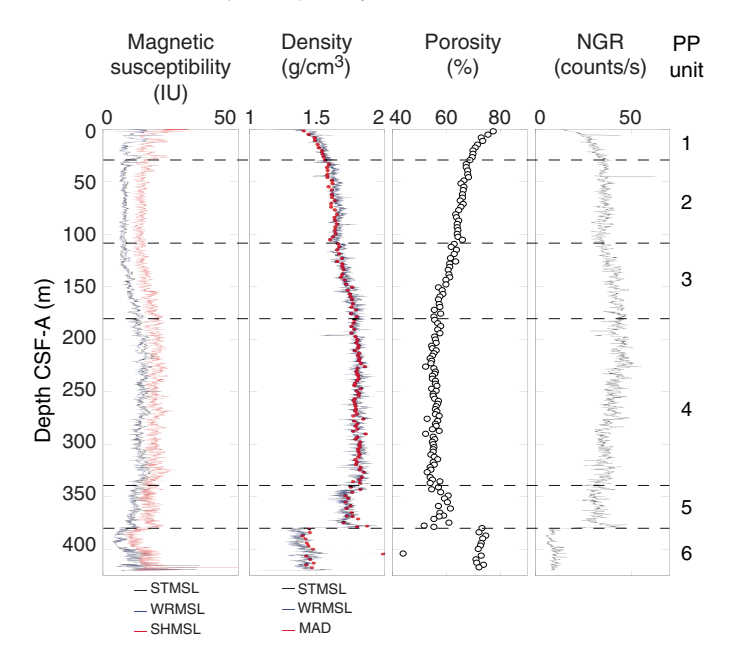
Natural gamma radiation

NGR counts in Hole U1448A range between 3.93 and 62.76 counts/s. There is low variability with an increasing trend downhole in PP Unit 1 from \sim 13.87 to 45.06 counts/s. PP Unit 2 counts steady out with an average of 35.2 counts/s. PP Unit 3 counts show and increasing trend relative to PP Unit 2 with an average of 40.57 counts/s. There is a slight jump to higher NGR counts at the PP Unit 3/4 boundary. PP Unit 4 shows high variability (22.62–55.45 counts/s) with an overall decreasing trend following the initial jump to higher counts. PP Unit 4 averages 39.62 counts/s. PP Unit 5 is generally steady at \sim 30.8 counts/s. There is a dramatic drop in NGR counts at the PP Unit 5/6 hiatus, indicating less clay content in PP

Table T14. Minimum, maximum, and mean statistics of measured physical property data, Holes U1448A–U1448C. MAD = moisture and density, SHMSL = Section Half Multisensor Logger, MS = magnetic susceptibility, NGR = natural gamma radiation, STMSL = Special Task Multisensor Logger, WRMSL = Whole-Round Multisensor Logger. **Download table in .csv format.**

Attribute	Minimum	Maximum	Mean
Hole U1448A:			
L*	28.1	51.6	39.72
a*	-1.9	1.7	0.34
b*	-3.7	7.2	-0.49
Red	9.4	74.9	49.19
Green	8.8	74.8	48.76
Blue	8.6	70.3	44.28
MAD density (g/cm ³)	1.4	1.99	1.7
STMSL density (g/cm ³)	1.1	1.95	1.7
WRMSL density (g/cm ³)	1.19	1.93	1.7
MAD porosity (%)	44.1	77.3	60.47
SMHSL MS (IU)	5.67	71.33	17.32
STMSL MS (IU)	3.85	35.9	11.78
WRMSL MS (IU)	3.33	34	11.11
NGR (counts/s)	5.56	63.03	35.13
Hole U1448B:			
L*	30	46.9	39.29
a*	-0.7	2.2	0.53
b*	-3.9	6.6	-0.36
Red	31.9	62.4	48.17
Green	31	63.9	47.77
Blue	27.9	60.6	43.38
STMSL density (g/cm ³)	1.19	1.67	1.54
WRMSL density (g/cm³)	1.35	1.89	1.7
WRMSL density (IU)	5	20	11.04
SMHSL MS (IU)	10.67	37	17.35
STMSL MS (IU)	4.27	21.79	11.17
NGR (counts/s)	13.14	53.42	38.16

Figure F23. Physical properties showing downhole variability in magnetic susceptibility from WRMSL, STMSL, and point SHMSL; density from WRMSL, STMSL, and MAD (red points); porosity; and NGR, Hole U1448A.



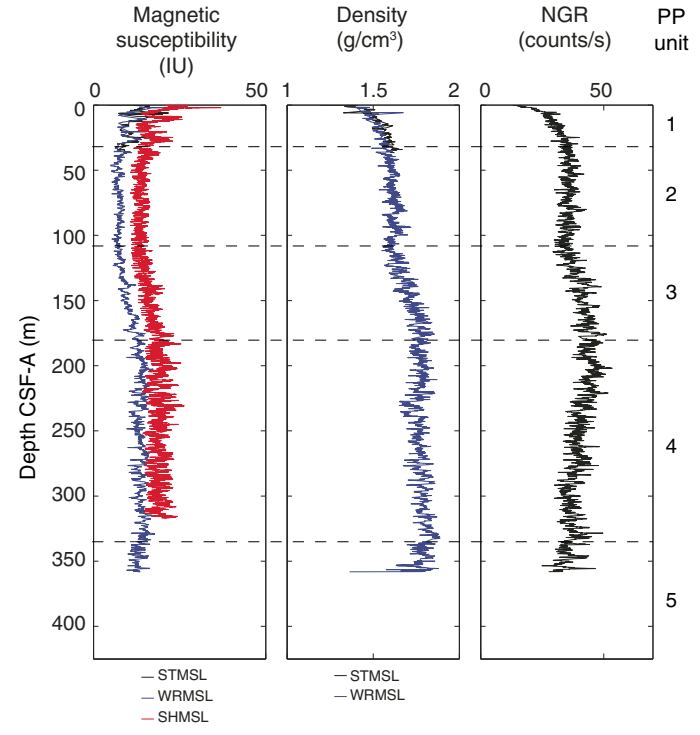
Unit 6, with an average of 9.63 counts/s (Figure **F23**). The long-term trends in NGR counts between PP Units 1 and 5 show cyclicity that is possibly related to variations in the input of terrigenous sediments.

GRA and MAD bulk density

The bulk density at Site U1448 was measured using (1) the GRA method using the WRMSL and STMSL for estimates from whole-round sections and (2) MAD measurements on discrete samples that provide a second, independent measure of bulk density and the dry density, grain density, water content, and porosity (Figures F23, F24, F25). The MAD and GRA data show excellent agreement. The GRA data between Holes U1448A and U1448B are also in excellent agreement; therefore, we discuss the data from the WRMSL and MAD measurements taken in Hole U1448A only.

Although the density data generally follow a linear increase with depth because of compaction, we still divide the data into the same six physical property units as the MS and NGR unit depths. The GRA bulk density values range from $\sim\!0.991$ to $1.94~g/cm^3$. Comparably, MAD bulk density ranges between 1.395 and 1.991 g/cm³ with mean density values of 1.705 g/cm³ (bulk) and 2.740 g/cm³ (grain). The minimum and maximum dry density is 0.611 and 1.539 g/cm³, respectively. Porosity decreases with depth in PP Units 1, 2, and 3 and levels off to an average of $\sim\!56\%$ in PP Unit 6. PP Unit 5 is characterized by an anomalous porosity increase up to 61.5% possibly from an increase in biosiliceous material (sponge spicules), and then there is an intense porosity increase below the hiatus in PP

Figure F24. Physical properties showing downhole variability in magnetic susceptibility from WRMSL, STMSL, and point SHMSL; density from WRMSL and STMSL; and NGR, Hole U1448B.



Unit 6. PP Unit 6 has an average porosity of 72.5%. The overall porosity ranges between 44.1% and 77.3%, whereas the volume of the pore water per 10 cm³ sample is between 1.885 and 8.162 cm³ with a mean value of 5.531 cm³ (Figure **F23**).

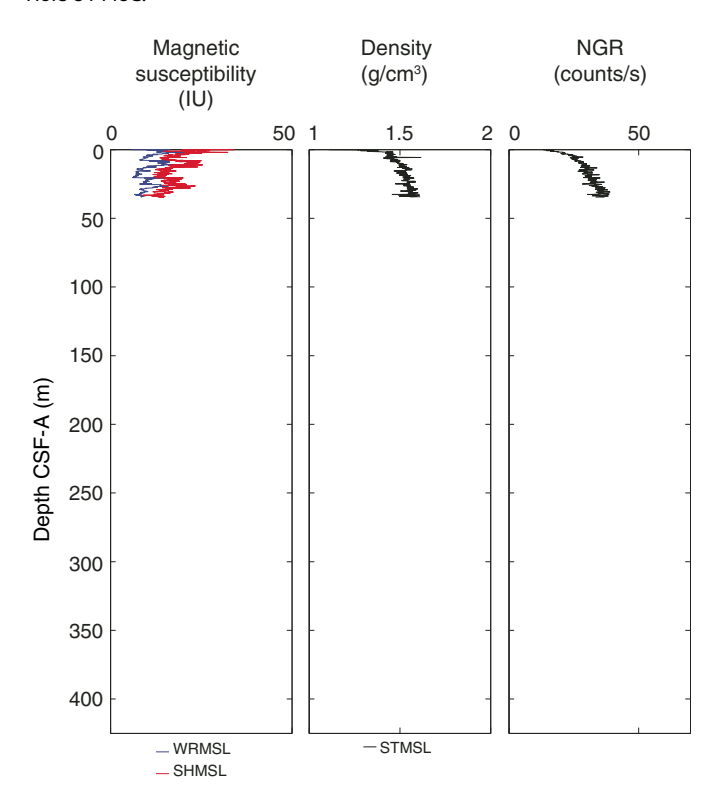
The average bulk density from GRA measurements for PP Units 1–5 are 1.49, 1.61, 1.69, 1.73, 1.62, and 1.39 cm³, respectively. Downcore, the minimum GRA bulk density is 0.901 cm³ and the maximum is 1.950 cm³ with an overall average of 1.682 cm³. A dramatic decrease in density with a corresponding dramatic increase in porosity occurs below the hiatus that demarks the PP Unit 5/6 boundary.

Diffuse reflectance spectroscopy and digital color image

Spectral reflectance was measured on all archive section halves using the SHMSL. There are slight color variations downhole with the most noticeable change related to a general lowering of the b* trend downcore until Hole U1448A PP Unit 6. There is little variation in a* and moderate to high variations in L*. PP Unit 1 shows high variation in all SHMSL values.

In Hole U1448A, L* ranges between 28.1 and 51.6 (average = 39.72) and reflectance a* and b* range between -1.9 and 1.7 (average = 0.34) and -3.7 and 7.2 (average = -0.49), respectively (Table T14; Figure F26). There is a stepwise change to lower L* values at the PP Unit 4/5 boundary and an increase in L* at the PP Unit 5/6 boundary. The PP Unit 1/2 boundary is not as distinct but rather is the beginning of a gradual downcore transition to lower b* values until the PP Unit 5/6 boundary. Downhole variability in L*, a*, and b* from Holes U1448B and U1448C are shown in Figures F27 and F28.

Figure F25. Physical properties showing downhole variability in magnetic susceptibility from WRMSL and point SHMSL, density from STMSL, and NGR, Hole U1448C.



SHIL data (RGB) were measured from the surface of the split archive halves prior to drying. In Hole U1448A, R ranges between 9.4 and 74.9 (average = 49.19), G ranges between 8.8 and 74.8 (average = 48.76), and B ranges between 8.6 and 70.3 (average = 44.28) (Table **T14**). A marked increase in R, G, and B counts occur at the PP Unit 5/6 boundary below the hiatus. (Figure **F29**). Between PP Units 1 and 5, the color data show cyclicity on short- and long-term time-scales. Downcore variability in RGB is also shown for Holes U1448B and U1448C (Figures **F30**, **F31**).

Figure F26. L*, a*, and b* data, Hole U1448A.

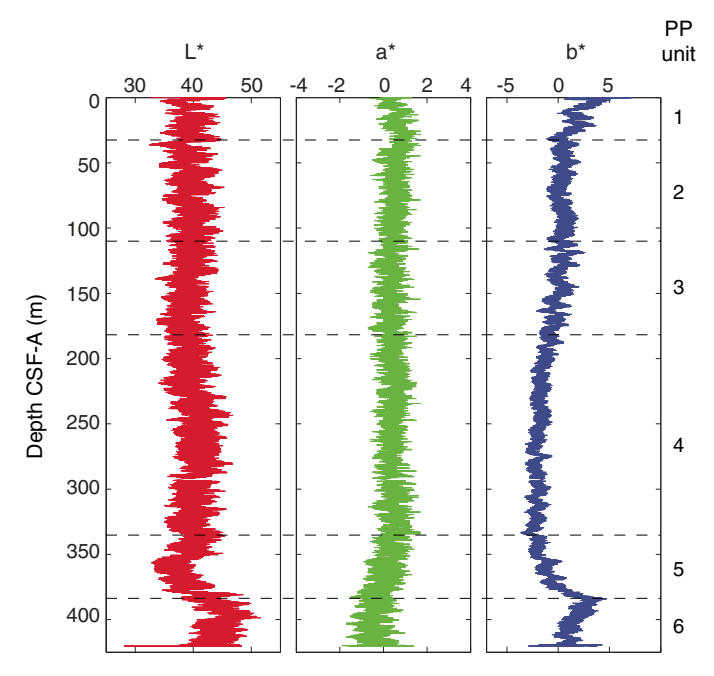


Figure F27. L*, a*, and b* data, Hole U1448B.

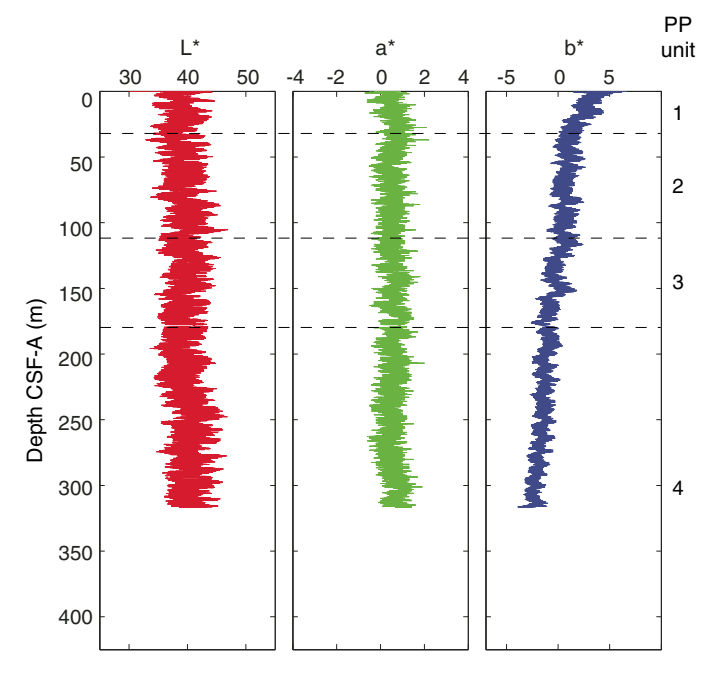


Figure F28. L*, a*, and b* data, Hole U1448C.

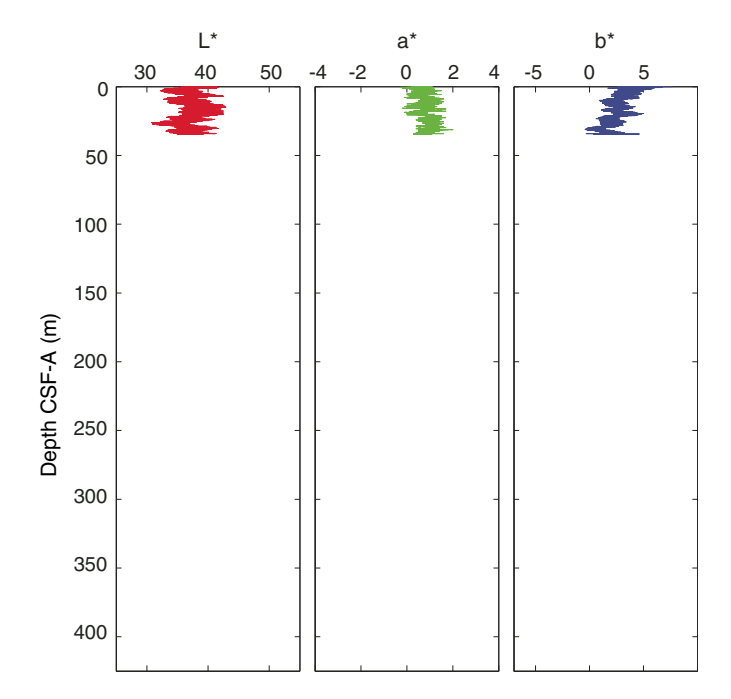
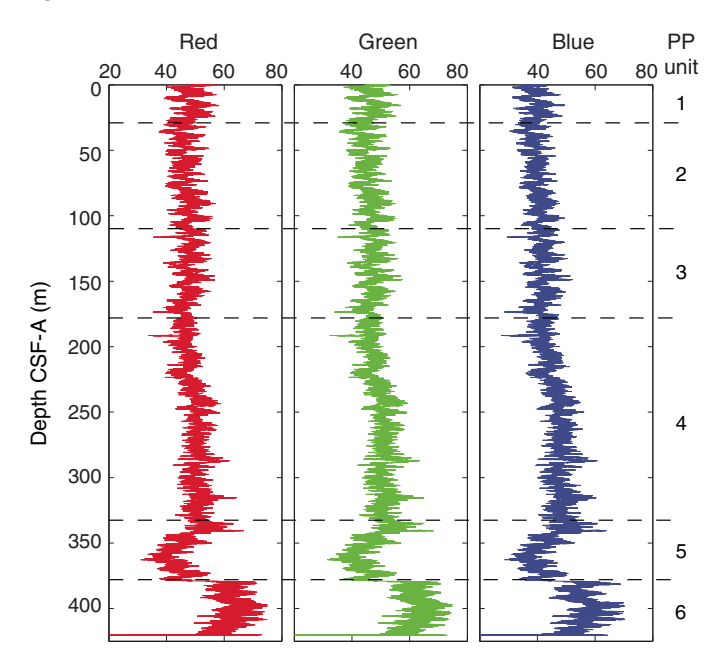


Figure F29. SHIL RGB color data, Hole U1448A.



Downhole temperature

Downhole temperature measurements were made on Cores 353-U1448B-4H, 7H, 10H, and 15H using the APCT-3 (Table **T15**). The geothermal gradient was calculated to be $\sim 20^{\circ}$ C/km (Figure **F32**).

Summary

We identified six physical property units in Hole U1448A. The data between Holes U1448A and U1448B correlate well. Many of the changes in physical property characteristics of Hole U1448A

Figure F30. SHIL RGB color data, Hole U1448B.

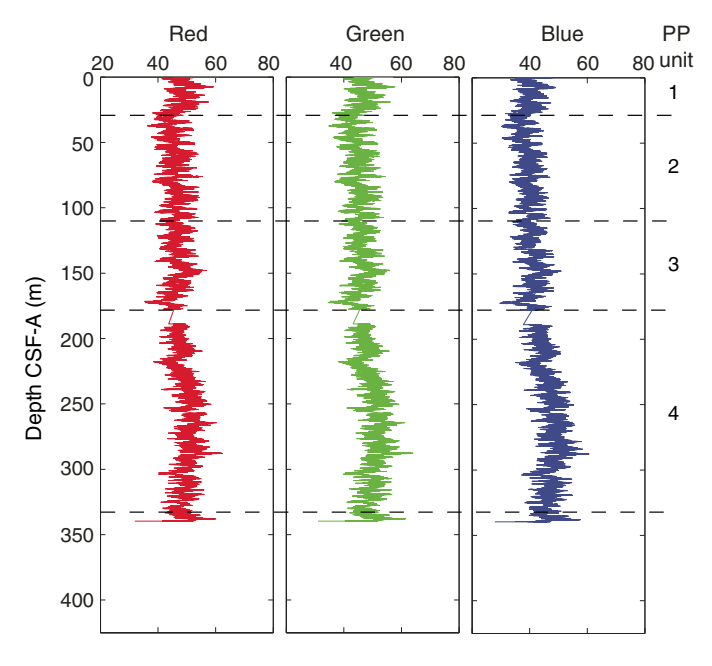
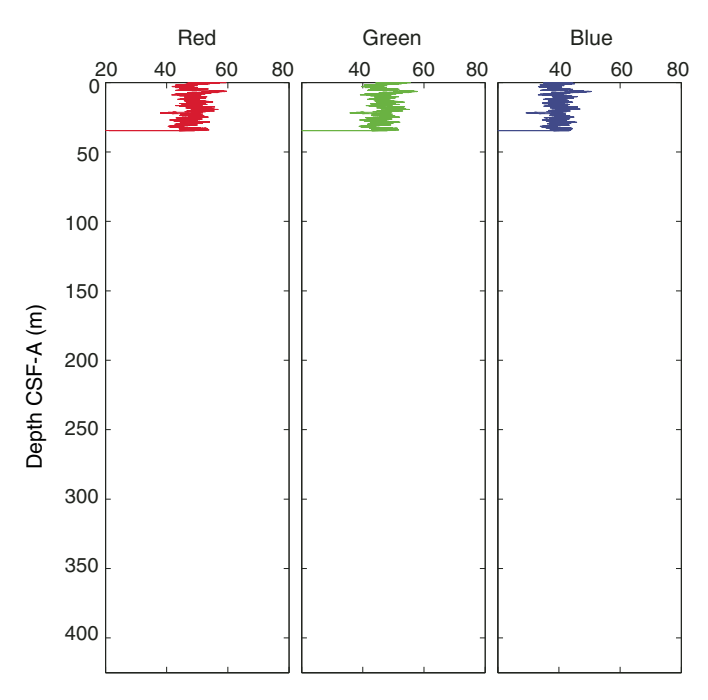


Figure F31. SHIL RGB color data, Hole U1448C.

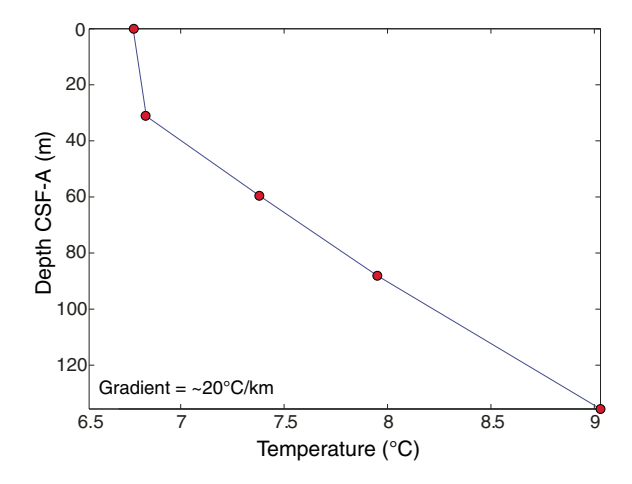


were gradual shifts to increasing or decreasing values. The NGR data were the only data to show long-term cyclicity, possibly related to cycles in terrigenous input. PP Unit 1 (0–30.9 m CSF-A) shows high variability in most measurements, likely related to the unconsolidated nature of the upper sediment column. PP Unit 2 (30.9–107.2 m CSF-A) shows little MS variability, increasing density, decreasing porosity, and relatively steady NGR counts. PP Unit 3 is characterized by an increase in MS, increase in density, increase in NGR counts, decrease in porosity, and lower b* values, indicating more terrigenous material and clay relative to carbonate or siliceous

Table T15. Downhole temperature data from the APCT-3, Hole U1448B. **Download table in .csv format.**

Depth CSF-A (m)	Temperature (°C)
0	6.7
30.99	6.83
59.53	7.38
88.05	7.95
135.58	9.03

Figure F32. Downhole temperature data, Hole U1448B.



fractions. PP Unit 4 (182.9–338.6 m CSF-A) corresponds to lithostratigraphic Unit II. It has steady high MS values, steady high density, a continued decrease in porosity, variable NGR counts, and the lowest b* values that transitions to a smaller PP Unit 5 (338.6–379.1 m CSF-A) where MS values decrease, density decreases, porosity increases, NGR counts decrease, and b* begins to increase. The physical properties of PP Unit 5 likely indicate an increase in abundance of more biosilica-rich clay (see **Lithostratigraphy**). Most noticeably, all physical property measurements showed a very dramatic change at 379.1 m CSF-A, which was determined to mark a ~8 My hiatus (see **Biostratigraphy**).

Stratigraphic correlation

A composite scale (CCSF-A) and a splice (CCSF-D) were constructed for Site U1448 using Holes U1448A–U1448C (as defined in **Stratigraphic correlation** in the Expedition 353 methods chapter [Clemens et al., 2016a]). Splicing among these holes enabled us to construct a continuous stratigraphic sequence to ~ 203 m CCSF-D (Tables **T16**, **T17**; Figure **F33**). Following a set gap, a floating composite scale was constructed between $\sim\!205$ and $\sim\!260$ m CCSF-A using Holes U1448A and U1448B (Table **T16**).

Table T16. Vertical offsets applied to cores in order to align structure in adjacent holes, Site U1448. **Download table in .csv format.**

Table T17. Splice intervals, Site U1448. Download table in .csv format.

Construction of CCSF-A scale

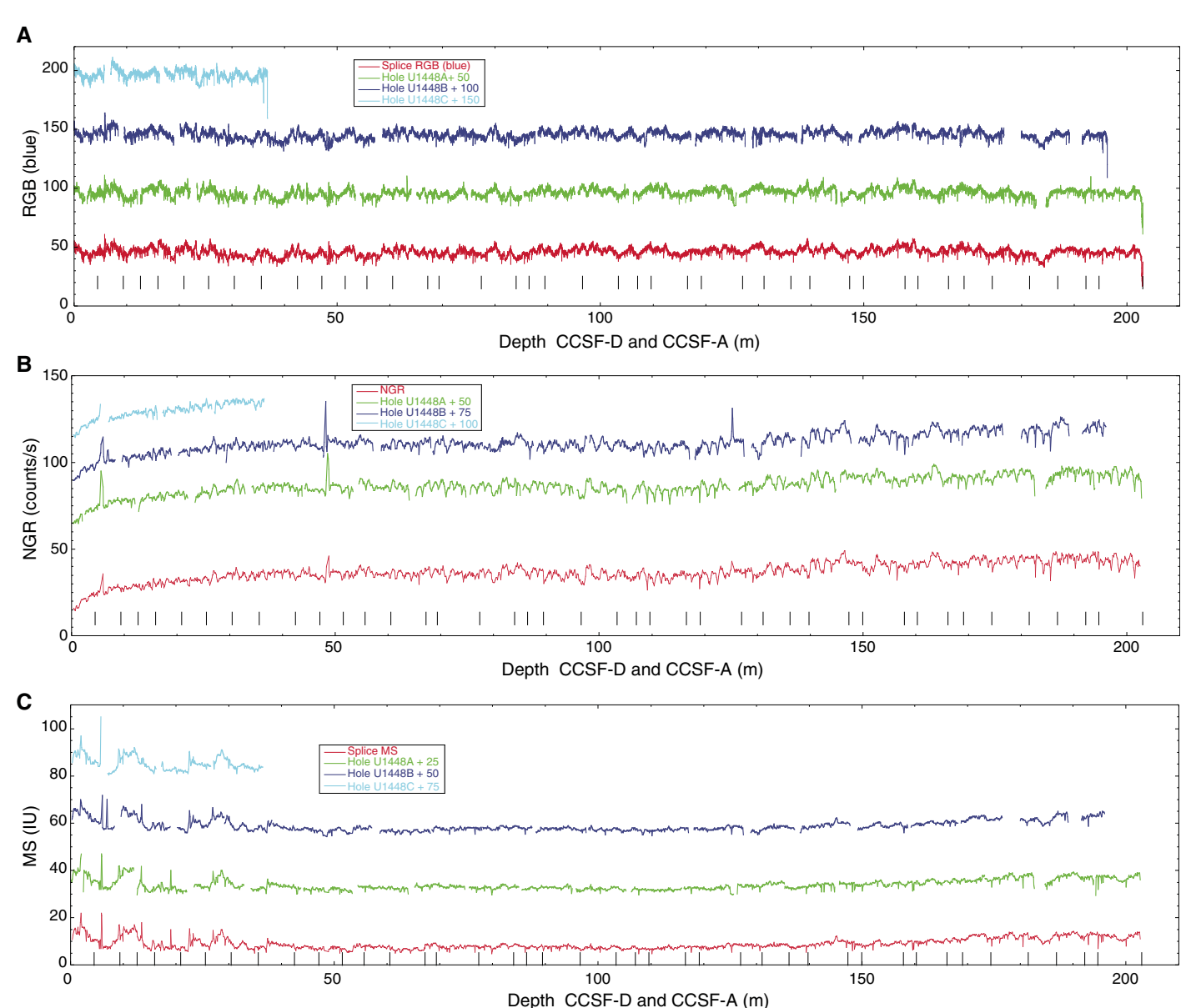
We selected the core with the best mudline recovery (Core 353-U1448C-1H) to anchor the composite depth scale and defined the top as 0 m CCSF-A. The CCSF-A scale for Site U1448 (see Table T16) is based on correlation of RGB color and secondarily on MS data. RGB green was utilized for correlations in Site U1448. MS was measured on whole-round sections, whereas green was measured on archive-half sections (see **Physical properties** for details). The R, G, and B components of the RGB triplet are highly correlated to each other because, on the first order, all are measures of the reflectivity of the sediment. The small differences between R, G, and B can be expressed as ratios such as red/green, red/blue, or green/blue. However, ratios were not employed in our correlation due to lack of time (see the **Expedition 353 methods** chapter [Clemens et al., 2016a]). Reflectance spectroscopy data (i.e., L*, a*, and b*), which can produce information similar to RGB ratios, were not used for correlation due to inconsistent variability from hole to hole resulting from low-quality wavelength spectra collected by the Ocean Optics USB4000 spectrophotometer on the monotonously dark sediments of Site U1448.

Construction of CCSF-D scale

A combination of Holes U1448A–U1448C cover the stratigraphic section to ~203 m CCSF-D. When constructing the splice, we tried to minimize inclusion of disturbed intervals and avoid whole-round sampling intervals (notably from Hole U1448A) as much as possible. Selected splice intervals are listed in Table T17. Postcruise, the splice interval tables were modified using the Splice-File-Fixer program to ensure that each depth has been assigned the correct sample ID. Both the affine and the corrected splice interval tables were uploaded into the Laboratory Information Management System (LIMS) during the first postcruise meeting in June 2015. The core top depths in the affine tables were not corrected and hence may be slightly incorrect in a range of <2 cm. However, the offsets are correct.

Reliance on RGB, which sometimes has fuzzy character due to cracks and defects of the split core surface, precluded, in places, the definition of a unique correlation. Features and general trends were used instead, reducing the accuracy of the splice to the decimeter range. As a result, correlation should be viewed with caution deeper than ~115 m CCSF-A, notably if high-resolution sampling is planned. Onshore X-ray fluorescence scanning, color reflectance rescanning, and bulk $\delta^{18}{\rm O}$ should provide better means of correlation.

Figure F33. Core alignment shown using (A) RGB blue (used in lieu of green due to availability of outlier-cleaned data), (B) NGR, and (C) MS profiles, Holes U1448A–U1448C. Spliced profile is also shown. Splice tie points are indicated by black vertical lines. Original KaleidaGraph files are available in STRATCOR in Supplementary material.



References

Awasthi, N., Ray, J.S., Singh, A.K., Band, S.T., and Rai, V.K., 2014. Provenance of the late Quaternary sediments in the Andaman Sea: implications for monsoon variability and ocean circulation. *Geochemistry, Geophysics, Geosystems*, 15(10):3890–3906.

http://dx.doi.org/10.1002/2014GC005462

Barron, J.A., 1985. Miocene to Holocene planktic diatoms. *In Bolli*, H.M., Saunders, J.B., and Perch-Nielsen, K. (Eds.), *Plankton Stratigraphy*: Cambridge, United Kingdom (Cambridge University Press), 763–809.

Bown, P.R. (Ed.), 1998. *Calcareous Nannofossil Biostratigraphy:* Dordrecht, The Netherlands (Kluwer Academic Publishing).

Clemens, S.C., Kuhnt, W., LeVay, L.J., Anand, P., Ando, T., Bartol, M., Bolton, C.T., Ding, X., Gariboldi, K., Giosan, L., Hathorne, E.C., Huang, Y., Jaiswal, P., Kim, S., Kirkpatrick, J.B., Littler, K., Marino, G., Martinez, P., Naik, D., Peketi, A., Phillips, S.C., Robinson, M.M., Romero, O.E., Sagar, N., Taladay, K.B., Taylor, S.N., Thirumalai, K., Uramoto, G., Usui, Y.,

Wang, J., Yamamoto, M., and Zhou, L., 2016a. Expedition 353 methods. *In* Clemens, S.C., Kuhnt, W., LeVay, L.J., and the Expedition 353 Scientists, *Indian Monsoon Rainfall*. Proceedings of the International Ocean Discovery Program, 353: College Station, TX (International Ocean Discovery Program). http://dx.doi.org/10.14379/iodp.proc.353.102.2016

Clemens, S.C., Kuhnt, W., LeVay, L.J., Anand, P., Ando, T., Bartol, M., Bolton, C.T., Ding, X., Gariboldi, K., Giosan, L., Hathorne, E.C., Huang, Y., Jaiswal, P., Kim, S., Kirkpatrick, J.B., Littler, K., Marino, G., Martinez, P., Naik, D., Peketi, A., Phillips, S.C., Robinson, M.M., Romero, O.E., Sagar, N., Taladay, K.B., Taylor, S.N., Thirumalai, K., Uramoto, G., Usui, Y., Wang, J., Yamamoto, M., and Zhou, L., 2016b. Site U1445. *In Clemens, S.C.*, Kuhnt, W., LeVay, L.J., and the Expedition 353 Scientists, *Indian Monsoon Rainfall*. Proceedings of the International Ocean Discovery Program, 353: College Station, TX (International Ocean Discovery Program). http://dx.doi.org/10.14379/iodp.proc.353.105.2016

Clemens, S.C., Kuhnt, W., LeVay, L.J., Anand, P., Ando, T., Bartol, M., Bolton, C.T., Ding, X., Gariboldi, K., Giosan, L., Hathorne, E.C., Huang, Y.,

- Jaiswal, P., Kim, S., Kirkpatrick, J.B., Littler, K., Marino, G., Martinez, P., Naik, D., Peketi, A., Phillips, S.C., Robinson, M.M., Romero, O.E., Sagar, N., Taladay, K.B., Taylor, S.N., Thirumalai, K., Uramoto, G., Usui, Y., Wang, J., Yamamoto, M., and Zhou, L., 2016c. Site U1447. *In Clemens*, S.C., Kuhnt, W., LeVay, L.J., and the Expedition 353 Scientists, *Indian Monsoon Rainfall*. Proceedings of the International Ocean Discovery Program, 353: College Station, TX (International Ocean Discovery Program). http://dx.doi.org/10.14379/iodp.proc.353.107.2016
- Colin, C., Turpin, L., Bertaux, J., Desprairies, A., and Kissel, C., 1999. Erosional history of the Himalayan and Burman ranges during the last two glacial-interglacial cycles. *Earth and Planetary Science Letters*, 171(4):647–660. http://dx.doi.org/10.1016/S0012-821X(99)00184-3
- Colin, C., Turpin, L., Blamart, D., Frank, N., Kissel, C., and Duchamp, S., 2006. Evolution of weathering patterns in the Indo-Burman Ranges over the last 280 kyr: effects of sediment provenance on ⁸⁷Sr/⁸⁶Sr ratios tracer. *Geochemistry, Geophysics, Geosystems*, 7(3):Q03007. http://dx.doi.org/10.1029/2005GC000962
- Collett, T.S., Riedel, M., Cochran, J., Boswell, R., Presley, J., Kumar, P., Sathe, A.V., Sethi, A., Lall, M., Sibal, V., and the NGHP Expedition 01 Scientists, 2008. *Indian National Gas Hydrate Program (NGHP) Expedition 01, Initial Report:* Noida, India (DGH, Ministry of Petroleum and Natural Gas).
- Curray, J.R., 1991. Possible greenschist metamorphism at the base of a 22-km sedimentary section, Bay of Bengal. *Geology*, 19(11):1097–1100. http://dx.doi.org/10.1130/0091-7613(1991)019<1097:PGMATB>2.3.CO;2
- Curray, J.R., 2005. Tectonics and history of the Andaman Sea region. *Journal of Asian Earth Sciences*, 25(1):187–232. http://dx.doi.org/10.1016/j.jseaes.2004.09.001

Flores, J.A., Johnson, J.E., Mejía-Molina, A.E., Álverez, M.C., Sierro, F.J., Singh, S.D., Mahanti, S., and Giosan, L., 2014. Sedimentation rates from calcareous nannofossil and planktonic foraminifera biostratigraphy in the Andaman Sea, northern Bay of Bengal, and eastern Arabian Sea. *Marine* and Petroleum Geology, 58(Part A):425–437.

- http://dx.doi.org/10.1016/j.marpetgeo.2014.08.011
- Frerichs, W.E., 1971. Planktonic foraminifera in the sediments of the Andaman Sea. *Journal of Foraminiferal Research*, 1(1):1–14. http://dx.doi.org/10.2113/gsjfr.1.1.1
- Gradstein, F.M., Ogg, J.G., Schmitz, M.D., and Ogg, G.M. (Eds.), 2012. *The Geological Time Scale 2012*: Amsterdam (Elsevier).
- Martini, E., 1971. Standard Tertiary and Quaternary calcareous nannoplankton zonation. *In Farinacci*, A. (Ed.), *Proceedings of the Second Planktonic Conference, Roma 1970*: Rome (Edizioni Tecnoscienza), 2:739–785.
- Okada, H., and Bukry, D., 1980. Supplementary modification and introduction of code numbers to the low-latitude coccolith biostratigraphic zonation (Bukry, 1973; 1975). *Marine Micropaleontology*, 5:321–325. http://dx.doi.org/10.1016/0377-8398(80)90016-X
- Singh, S.C., Moeremans, R., McArdle, J., and Johansen, K., 2013. Seismic images of the sliver strike-slip fault and back thrust in the Andaman-Nicobar region. *Journal of Geophysical Research: Solid Earth*, 118(10):5208–5224. http://dx.doi.org/10.1002/jgrb.50378
- Varkey, M.J., Murty, V.S.N., and Suryanarayana, A., 1996. Physical oceanography of the Bay of Bengal and Andaman Sea. *Oceanography and Marine Biology*, 34:1–70. http://drs.nio.org/drs/handle/2264/2276